7-3-2014

Analysis of the Ping-Pong Ball Gun-Theoretical & Computational Approach

JUN HAN BAE
bae21@purdue.edu

PURDUE
UNIVERSITY

Purdue University West Lafayette, Indiana

College of Technology

ANALYSIS OF THE PING-PONG BALL GUN – THEORETICAL & COMPUTATIONAL APPROACH

In partial fulfillment of the requirements for the
Degree of Master of Science in Technology

A Directed Project Report

By

Jun Han Bae

Committee Member	Approval Signature	Date
Richard M. French, Chair	Mark French	7/2/14
Nancy L. Denton	Nancy L Denton	6/30/2014
Eric T. Matson	Eric T Matson	7/2/2014

TABLE OF CONTENTS

Page

LIST OF TABLES

LIST OF FIGURES

Figure Page

Appendix Figure

ABSTRACT

Bae, Jun Han. M.S., Purdue University, August 2014. Analysis of the Ping-Pong Ball Gun – Theoretical & Computational Approach. Major Professor: Richard M. French.

A Ping-Pong ball gun test is simulated using computational fluid dynamics software, ‘Autodesk Simulation CFD 2014’. The ball velocity profile and airflow distribution are analytically predicted. The predicted responses are verified using the concepts of fluid mechanics and gas dynamics. In this paper, the development of the analytical model, analysis results, and theoretical approximation are presented. The analysis results and theoretical approximation demonstrate that the ball velocity profile of a basic Ping-Pong ball gun test can be theoretically approximated. In addition, no clear influence of the mesh size on the fundamental behavior of the gun can be observed.

CHAPTER 1. INTRODUCTION

1.1 Ping-Pong Ball Gun

A Ping-Ping ball gun is a vacuum - powered apparatus. It is often used in experiments in physics and mechanical engineering classes. (Cockman, 2003; French, Gorrepati, Alcorta, & Jackson, 2008; Peterson, Pulford, & Stein, 2005). Figure 1.1 shows an image of the gun. This device shoots a Ping-Pong ball with an exit velocity close to the speed of sound due to atmospheric pressure (French, Gorrepati, Alcorta, & Jackson, 2008). A simple modification is often required to the apparatus to achieve the exit velocity greater than the speed of sound. (French, Zehrung, & Stratton, 2013).

The Ping-Pong ball gun experiments have been performed in many physics and engineering classes in the past (Cockman, 2003; Pulford & Stein, 2004; Taylor, 2006; Olson, et al., 2006; Mungan, 2009). Analytical analyses have been also conducted to verify the experimental results. The verification analyses were performed based on related theories in physics and fluid mechanics.

It often requires computational fluid dynamics to describe the mechanism of the Ping-Pong ball gun precisely. Autodesk Simulation CFD 2014, a commercially available finite element analysis solver, is used to estimate the airflow and predict the velocity profile of the Ping-Pong ball.

1.2 Types of the Ping-Pong Ball Gun

There are two types of the Ping-Pong ball guns. They are basic Ping-Pong ball gun and modified Ping-Pong gun. The basic Ping-Pong gun is a single pipe with the diaphragm each end of the pipe. The pipe length is approximately 2.5m and the diameter of the pipe is 0.044m (44mm). The diameter of the Ping-Pong ball is 0.04m (40mm). Figure 1.2 shows the schematic drawing of the basic model. The modified Ping-Pong gun is a single pipe (same as the basic model) with a pressure plenum and a converging-diverging nozzle attached to the pipe. Figure 1.3 shows the schematic drawing of the modified model. The main difference between these two types is that the ball velocity at the end of the pipe. The ball velocity less than the speed of sound (subsonic) is achieved using the basic Ping-Pong gun while the ball velocity greater than the speed of sound (supersonic) is achieved using the modified Ping-Pong gun.

The ball velocity greater than the speed of sound is attainable using the pressure chamber and converging-diverging nozzle. The two ends of the pipe are sealed. The air inside of the pipe is ideally vacuum condition and the chamber is compressed to a certain level. This eventually differentiates the air pressure between the chamber and the pipe. When the diaphragm is punctured airflow goes through the converging – diverging nozzle and finally the ball is accelerated to supersonic speeds. More details will be presented in Chapter 3. Both experimental and analytical studies have been conducted for the basic Ping-Pong ball gun (details in Chapter 2). However, the experimental data for the modified Ping-Pong ball gun is somewhat limited. Only the exit velocity of the ball has been measured using the modified Ping-Pong gun so far. Therefore, an additional

study is required to investigate the fundamental behavior and response of the modified Ping-Pong ball.

The objectives of this research are (1) development of the analytical models to predict the ball velocity profile and the airflow inside of the pipe (2) verify the analytical model predictions with theoretical approximations.

1.3 Research Scope

Two modifications were done from the basic model to the modified model. It was the pressure difference divided by the diaphragm and addition of the converging-diverging nozzle. To make one modification at a time, the basic_2 model was introduced. The difference between the basic model and the basic_2 model is the pressure difference at the inlet of the pipe. Figure 1.4 shows three different type of the analysis model.

Analysis on the three different analytical models was conducted to estimate the ball velocity profile and the distribution of the airflow inside the pipe. The analysis was conducted using commercially available computational fluid dynamics simulation tool, Autodesk Simulation CFD 2014. The analytically predicted results were compared with the theoretical approximations to verify the results. However, the ball velocity profile for the modified Ping-Pong ball gun could not be theoretically approximated since the ball speed exceeds the speed of sound in the pipe. That is, the theory applied for the basic Ping-Pong ball gun is not applicable to the modified Ping-Pong ball gun anymore. As a result, the analytically predicted ball velocity profile of only the basic Ping-Pong ball gun was verified with the theoretical approximation.

Figure 1.1 The Ping-Pong ball gun

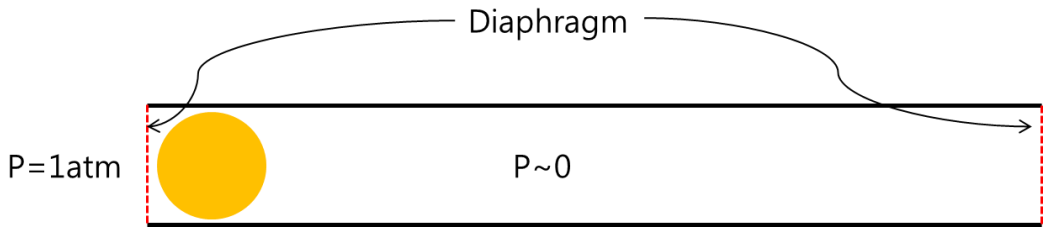

Figure 1.2 The basic model of the Ping-Pong ball gun

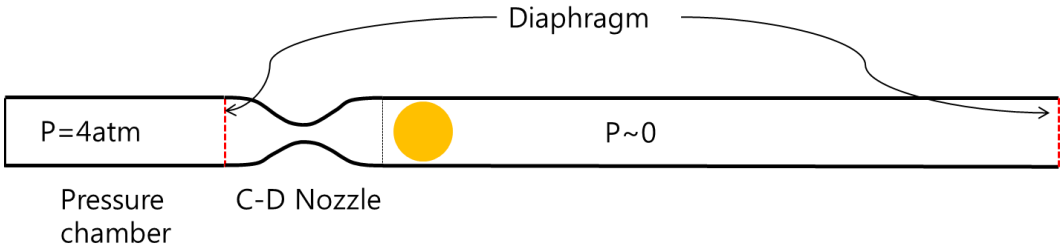

Figure 1.3 The modified model of the Ping-Pong ball gun

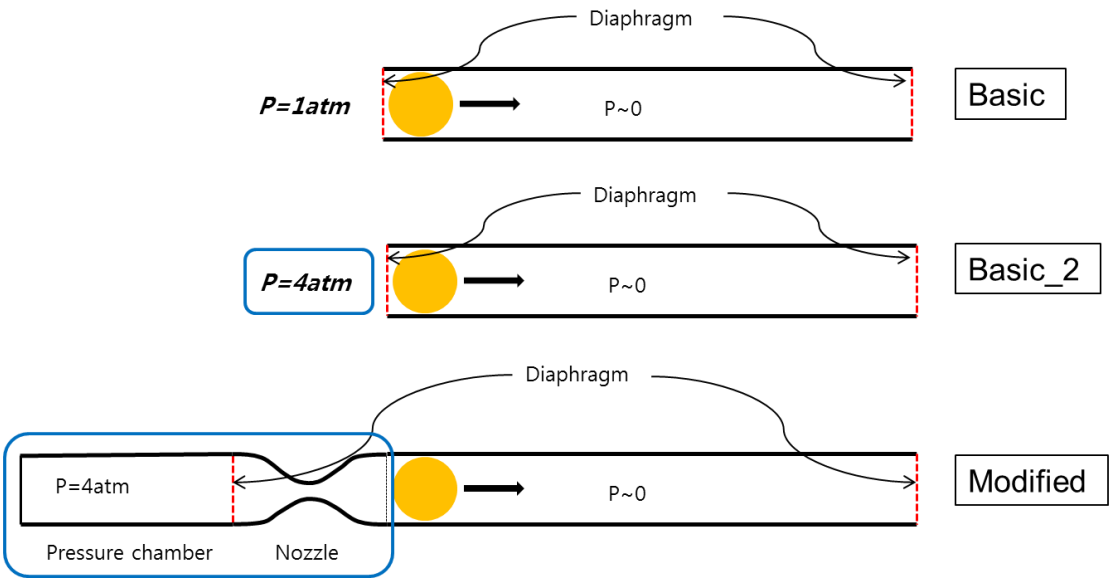

Figure 1.4 Three different types of the analysis model

CHAPTER 2. PREVIOUS WORK

Both analytical and experimental studies on a basic Ping-Pong ball gun were conducted by French, et al., 2008. The study mainly focused on the velocity profile of the ball. First, the ball velocity profile was theoretically approximated. The approximation was performed based on Newton's second law of motion. The authors assumed the pressure acting behind the ball is not constant. The authors reported the predicted ball velocity profile along the pipe (French, Gorrepati, Alcorta, & Jackson, 2008). More details about the theory are discussed in Chapter 3.

The analytical model simulation and the experiment were done from the previous work to increase the accuracy of the analysis and verify the results (French, Gorrepati, Alcorta, & Jackson, 2008). ANSYS FLUENT was used to obtain a precise airflow analysis. ANSYS FLUENT is the most common use simulation solver for computational fluid dynamic analysis. Dynamic mesh option was applied to calculate the ball motion (French, Gorrepati, Alcorta, & Jackson, 2008). The geometry of the Ping-Pong ball gun assumed that the ball diameter of 40mm and the pipe inner diameter of 44mm. The contour plot of the velocity and the pressure distribution inside of the pipe was shown. From the figure of the simulation results, the normal shock was observed at the gap between the ball and the pipe (French, Gorrepati, Alcorta, & Jackson, 2008). The velocity profile result of the ball was verified by the predicted velocity as a function of

displacement from theoretical approximation. However, comparing results from the two different approaches were limited to the short length (from 0m to 0.035m). Experimental verification was done to compare with the theoretical approximation. The schedule 40 PVC pipe was used for the barrel. A Piezotronics PCB pressure sensor, laser diodes and high-speed photo detectors on the three arbitrary locations were installed to collect data. It showed the prediction for the velocity as a function of the displacement with experiment data.

An experiment of the modified model was conducted by French, et al., 2013. The exit velocity of the ball was measured and its velocity was over Mach 1. The detail of the experiment setting was introduced. However, collecting only an exit velocity of the ball was the limitation of this experiment.

CHAPTER 3. METHODOLOGY

3.1 Development of Analytical Models

Analytical models were developed to simulate the airflow distribution and the ball velocity profile of a Ping-Pong ball gun in two dimensions. The models were developed using commercially available computational fluid dynamics software, Autodesk Simulation CFD 2014. They were developed for both basic and modified Ping-Pong ball guns.

3.1.1 Analysis Conditions

All parts of the analytical models were developed using Solidworks and they were exported to Autodesk Simulation CFD 2014. The material properties and boundary conditions reported by French, et al., 2008 were applied to the models. More details of the models are presented in the following sub-sections.

Material Properties

The material type and the volume inside the pipe was 'air with a pressure of 0.3 psi' (0.3psi is medium vacuum condition). It was the same pressure condition given in the test conducted by French, et al., 2008. The Ping-Pong ball was made of polyvinyl chloride (PVC). The common density value of PVC was used and it is 80.572 kg/m^3.

Boundary Conditions

The geometry of the Ping-Pong guns was symmetric along the length of the pipe. For this reason, symmetric boundary conditions were applied to the analytical models. A 'slip/symmetry' option was applied on bottom edges of the models. For the inlet condition, the pressure with 1atm was applied. The air pressure of 0.3 psi was applied on the exterior surface of the pipe and the outlet. For analytical models for the modified Ping-Pong ball gun, the same boundary conditions were applied. However, the air pressure of 4 atm was applied to the inlet.

Mesh

The computational fluid dynamics calculation is influenced by the mesh size in general. In this simulation, the mesh size varied from 1 to 0.2, to identify the influence of the mesh size on the analysis results. All elements were triangles since the models were analyzed in two dimensions. The corners and edges of the models were refined using the 'enhancement' function of the software.

Motion

The ball started move by airflow generated by the pressure different. The ball motion is modeled using the 'flow-driven' option.

3.1.2 Analysis Characteristics

Compressible Flow

Compressible flow analysis is for the Mach number of the airflow is greater than Mach 0.3 (velocity of air over *100m/s*). Since the normal shock generated and airflow inside of the pipe is supersonic flow, 'compressible flow' option was used in the analytical model analysis.

Turbulent Model

Since airflow inside of the pipe were compressible and high Reynolds number flow, turbulent model analysis was applied to the analytical model analysis. The governing equation of the turbulent model which used for the calculation shows as Equation 3.1 and 3.2.

$$\frac{\partial(\rho k)}{\partial t}+\frac{\partial(\rho k u_i)}{\partial x_i}=\frac{\partial}{\partial x_j}\left[\left(\mu+\frac{\mu_t}{\sigma_k}\right)\frac{\partial k}{\partial x_i}\right]+P_k+P_b-\rho\epsilon-Y_M+S_k \qquad (3.1)$$

$$\frac{\partial(\rho \epsilon)}{\partial t}+\frac{\partial(\rho \epsilon u_i)}{\partial x_i}=\frac{\partial}{\partial x_j}\left[\left(\mu+\frac{\mu_t}{\sigma_\epsilon}\right)\frac{\partial k}{\partial x_i}\right]+C_{1\epsilon}\frac{\epsilon}{K}(P_k+C_{3\epsilon}P_b)-C_{2\epsilon}\rho\frac{\epsilon^2}{k}+S_\epsilon \qquad (3.2)$$

Equation 3.1 and 3.2 is the governing equations of the k-epsilon turbulent model. It is default turbulent model for the computational fluid dynamics calculation.

Transient Analysis

'Transient analysis' was selected as a solution mode since this simulation involves unsteady flow. That is, a very small time-step size was needed. Time-step size of 0.00001s was selected and adequate time steps were decided as a number of iteration.

3.2 Theoretical Approximation

After the diaphragm is punctured, air at atmospheric pressure rush into the pipe and drives the Ping-Pong ball to the end of the pipe. Ideally, there should be no air in front of the Ping-Pong ball and no resistance caused by air drag. The ball, therefore, accelerates quickly down to the pipe. However, in the actual Ping-Pong ball gun, the in-diameter of the pipe is slightly larger than the ball diameter. A small amount of air passed through a very thin gap between the ball and the inner wall of the pipe. It propagates to the end of the pipe and gets compressed. As a result, the pressure between the ball and the diaphragm increases and the diaphragm ruptures (French, Gorrepati, Alcorta, & Jackson, 2008).

3.2.1 The Ball Velocity Function of the Basic Model

Newton's second law of motion is given in Equation 3.3. In the equation, P_0 is the air pressure at the inlet (x = 0), ρ is air density, A is the cross-sectional area of the ball, and v is the ball velocity. When Equation 3.3 is integrated, Equation 3.4 is produced. In Equation 3.4, m is the mass of the ball. For the simplification, $\frac{m}{\rho A}$ is defined as a characteristic length, λ. Equation 3.4, then, is simplified as Equation 3.5.

$$P_0 A = \frac{d}{dt}[(m + \rho x A)v] \tag{3.3}$$

$$P_0 A t = m\left(1 + \frac{\rho x A}{m}\right)v \tag{3.4}$$

$$P_0 A t = m\left(1 + \frac{x}{\lambda}\right)v \tag{3.5}$$

If Equation 3.5 is integrated, the equation is rearranged as Equation 3.6. The solution of the equation is easily found as Equation 3.7. Equation 3.7 is the displacement

of the ball as a function of time, *t*. By differentiating equation 3.8, the ball velocity is calculated as given in Equation 3.8.

$$\frac{1}{2}P_0At^2 = m\left(x + \frac{x^2}{2\lambda}\right) \tag{3.6}$$

$$x(t) = \lambda\left[\sqrt{1 + \frac{a_o t^2}{\lambda}} - 1\right] \tag{3.7}$$

$$v(t) = \frac{dx}{dt} = \frac{a_o t}{\sqrt{1+\frac{a_o t^2}{\lambda}}} \tag{3.8}$$

In Equation 3.8, when *t* approaches infinity, the maximum velocity (v_{max}) is calculated as Equation 3.9. When the equation is rearranged in the asymptotic form, Equation 3.10 is produced. The theoretically approximated maximum velocity of the ball calculated using Equation 3.10 for the basic model is 287.61 m/s. If Equation 3.6 is substituted into Equation 3.10, the ball velocity as a function of displacement can be calculated as Equation 3.11.

$$v_{max} \equiv \sqrt{a_o\lambda} = \sqrt{\frac{P_0}{\rho}} \tag{3.9}$$

$$v(t) = \frac{v_{max}}{\sqrt{1+\frac{\lambda}{a_o t^2}}} \tag{3.10}$$

$$v(x) = v_{max}\left[\frac{x}{x+\lambda}\sqrt{1 + 2\frac{\lambda}{x}}\right] \tag{3.11}$$

Equation 3.11 is the general form of the ball velocity function of displacement for the basic model.

3.2.2 Theoretical Approximation for the Modified Model

As mentioned in Chapter 1, the theoretical approximation of the ball velocity for the modified model wasn't analyzed. For the modified model, it was not possible to apply the first-order approximation that used for the basic model. The ball velocity exceeded the theoretical maximum velocity and the converging-diverging nozzle was attached. It is very complicate to predict the airflow inside of the converging-diverging nozzle. A new theoretical approximation will be required and leave this problem as a future work.

CHAPTER 4. ANALSIS RESULTS

A Ping-Pong ball gun test was simulated using Autodesk Simulation CFD 2014. Since it involves high-Reynolds number, compressible flow, and turbulent airflow, simulating the test was quite challenging. The analytical models described in the previous sections were used to predict the airflow distribution through the pipe and velocity profile of the ball.

The airflow distribution and the ball velocity profile were analytically predicted for the full length (approximately 2.5 m) of the Ping-Pong ball pipe. The predicted ball velocity profile was reasonable and close to the theoretical approximation. However, the predicted airflow distribution through the pipe was not realistic. The values of the air velocity and pressure were too large at some locations. The cause of this unrealistic and this strange phenomenon was not clear. For this reason, the simulation focused on a limited length (up to 0.05 m from the inlet). The analysis results are presented in the following sub-sections.

4.1 Analytical Model Results – Basic Model

As stated in Chapter 3, five different mesh sizes were considered in this study. Figure 4.1 shows analytical models with five different mesh sizes. As shown in the figure, the mesh size 1 was the coarsest mesh size and the mesh size 0.2 was the finest mesh size.

4.1.1 Airflow Distribution of the Basic Model

Mesh size 1

Figure 4.2 shows the airflow velocity and pressure distributions of the model with the mesh size 1. The figure shows the distributions when the ball was located at x = 0m, x = 0.025m, and x = 0.05m. The ball moved 0.025m within 0.00177s and moved 0.05m within 0.00212s. As shown in the figure, as the air is released, it propagates through the pipe and the airflow velocity increases. In addition, some sharp-edges are identified in the velocity profile. The air pressure should show the similar distribution to the airflow velocity distribution. However, the air pressure appears to show no relevance to the velocity distribution.

Mesh size 0.8

Figure 4.3 shows the airflow velocity and pressure distributions of the model with the mesh size 0.8. The figure shows the distributions when the ball was located at x = 0m, x = 0.025m, and x = 0.05m. The ball moved 0.025m within 0.00180s and moved 0.05m within 0.00229s.The analytically predicted distributions are very similar to what is shown in Figure 4.2. However, the velocity contour plot shows less sharp edges compared to the mesh size 1.

Mesh size 0.6 & 0.4

Figure 4.4 shows the airflow velocity and pressure distributions of the model with the mesh size 0.6. The ball moved 0.025m within 0.00284s and moved 0.05m within

0.00374s. Figure 4.5 shows the airflow velocity and pressure distributions of the model with the mesh size 0.4. The ball moved 0.025m within 0.00211s and moved 0.05m within 0.00284s. As shown in the figures, a shock wave at the entrance of the pipe appears to be identified. In addition, the distributions are captured more smoothly as the mesh size gets smaller. However, the model with the smaller mesh size shows reduction in the amount of the air pass through the gap between the ball and the pipe wall.

Mesh size 0.2

Figure 4.6 shows the airflow velocity and pressure distributions of the model with the mesh size 0.2. The ball moved 0.025m within 0.00154s and moved 0.05m within 0.00188s. A clear shock wave at the entrance of the pipe is identified from the airflow velocity contour plot. However, only a little amount of the air passes around the ball when the ball located at x = 0.05m. An irregular shape was observed on the pressure distribution compared to the velocity profile.

4.1.2 Velocity Profile of the Basic Model

Ball Velocity - Displacement Response

Figure 4.7 shows the ball velocity – displacement responses predicted using the analytical models with different mesh sizes. The velocity increases as the ball moves away from the inlet in general. However, it appears that there is no tendency between the mesh size and the response. Table 4.1 presents analytically predicted ball velocity at x = 0.025m and 0.05m for different mesh sizes. The predicted ball velocity varies from

25.7804 m/s to 69.9296 m/s at x = 0.025m and varies 28.9388m/s to 84.0754m/s at x = 0.005m . The tendency between the mesh size and the ball velocity response is not clear.

Ball Velocity – Time Response

Figure 4.8 shows the analytically predicted ball velocity – time responses for different mesh sizes. As shown, the ball velocity increases as time elapses in general. However, no clear tendency is observed. Table 4.2 presents analytically predicted ball velocity at the elapsed time t = 0.001sec. and t = 0.002sec. for different mesh sizes. Again, no clear influence of the mesh size is identified.

Displacement – Time Response

Figure 4.9 shows the analytically predicted ball displacement – time responses for different mesh sizes. As shown in the figure, no clear influence of the mesh size on the response is observed. Table 4.3 presents analytically predicted ball displacement at the elapsed time t = 0.001sec. and t = 0.002sec. for different mesh sizes. The analytically predicted ball displacement varies from 0.001 to 0.004 at t = 0.001 sec. and varies from 0.020 to 0.060 at t = 0.002 sec.

4.2 Analytical Model Results – Basic_2 Model

Same as the basic model, analytical model analysis of the basic_2 model was conducted with five different mesh sizes.

4.2.1 Airflow Distribution of the Basic_2 Model

Mesh size 1

Figure 4.10 shows the airflow velocity and pressure distributions of the model with the mesh size 1. The figure shows the distributions when the ball was located at x = 0m, x = 0.025m, and x = 0.05m. The ball moved 0.025m within 0.00177s and moved 0.05m within 0.00215s. As shown in the figure, as the air is released, it propagates through the pipe and the airflow velocity increases.

Mesh size 0.8

Figure 4.11 shows the airflow velocity and pressure distributions of the model with the mesh size 0.8. The figure shows the distributions when the ball was located at x = 0m, x = 0.025m, and x = 0.05m. The ball moved 0.025m within 0.00190s and moved 0.05m within 0.00264s.

Mesh size 0.6 & 0.4

Figure 4.12 shows the airflow velocity and pressure distributions of the model with the mesh size 0.6. The ball moved 0.025m within 0.00089s and moved 0.05m within 0.00110s. Figure 4.13 shows the airflow velocity and pressure distributions of the model with the mesh size 0.4. The ball moved 0.025m within 0.00084s and moved 0.05m within 0.00105s. As shown in the figures, a shock wave at the entrance of the pipe appears to be identified. In addition, the distributions are captured more smoothly as the mesh size gets smaller.

Mesh size 0.2

Figure 4.14 shows the airflow velocity and pressure distributions of the model with the mesh size 0.2. The ball moved 0.025m within 0.00084s and moved 0.05m within 0.00105s. A clear shock wave at the entrance of the pipe is identified from the airflow velocity contour plot. However, only a little amount of the air passes around the ball when the ball located at x = 0.05m. An irregular shape was observed on the pressure distribution compared to the velocity profile.

4.2.2 Velocity Profile of the Basic_2 Model

Ball Velocity - Displacement Response

Figure 4.15 shows the ball velocity – displacement responses predicted using the analytical models with different mesh sizes. The velocity increases as the ball moves away from the inlet in general. However, it appears that there is no tendency between the mesh size and the response. Table 4.4 presents analytically predicted ball velocity at x = 0.025m and 0.05m for different mesh sizes. The predicted ball velocity varies from 29.1244 m/s to 104.938 m/s at x = 0.025m and varies 36.9561 m/s to 134.808 m/s at x = 0.005m . The tendency between the mesh size and the ball velocity response is not clear.

Ball Velocity – Time Response

Figure 4.16 shows the analytically predicted ball velocity – time responses for different mesh sizes. As shown, the ball velocity increases as time elapses in general. However, no clear tendency is observed. Table 4.5 presents analytically predicted ball

velocity at the elapsed time t = 0.001sec. and t = 0.002sec. for different mesh sizes. Again, no clear influence of the mesh size is identified.

Displacement – Time Response

Figure 4.17 shows the analytically predicted ball displacement – time responses for different mesh sizes. As shown in the figure, no clear influence of the mesh size on the response is observed. Table 4.6 presents analytically predicted ball displacement at the elapsed time t = 0.001sec. and t = 0.002sec. for different mesh sizes.

4.3 Analytical Model Results – Modified Model

The modified Ping-Pong ball gun test was also simulated using the analytical models. Again, five different mesh sizes were considered in this study. Figure 4.18 shows analytical models of the modified model with five different mesh sizes. As shown in the figure, the mesh size 1 was the coarsest mesh size and the mesh size 0.2 was the finest mesh size.

4.3.1 Airflow Distribution of the Modified Model

Mesh size 1

Figure 4.19 shows the airflow velocity and pressure distributions of the model with the mesh size 1. The figure shows the distributions when the ball was located at x = 0 m, x = 0.025 m, and x = 0.05 m. The ball moved 0.025 m within 0.00201 sec. and moved 0.05 m within 0.00224 sec. The irregular contour plot was observed on the velocity distribution according to the coarse mesh and sharp-edge nozzle geometry. It

was possible to observe that air with 4atm pressure moved into the pipe on the pressure distribution. The air pressure should show the similar distribution to the airflow velocity distribution. However, the air pressure appears to show no relevance to the velocity distribution.

Mesh size 0.8

Figure 4.20 shows the airflow velocity and pressure distributions of the model with the mesh size 0.8. The figure shows the distributions when the ball was located at x = 0m, x = 0.025m, and x = 0.05m. The ball moved 0.025m within 0.00211s and moved 0.05m within 0.00231s. The velocity distribution of mesh size 0.8 shows a clear but angled shock wave at the entrance of the pipe. High velocity distribution was shown inside of the nozzle and low velocity distribution showed close to the front surface of the ball. The air pressure should show the similar distribution to the airflow velocity distribution. However, the air pressure appears to show no relevance to the velocity distribution.

Mesh size 0.6 & 0.4

Figure 4.21 shows the airflow velocity and pressure distributions of the model with the mesh size 0.6. The figure shows the distributions when the ball was located at x = 0m, x = 0.025m, and x = 0.05m. The ball moved 0.025m within 0.00219s and moved 0.05m within 0.00239s. Figure 4.22 shows the airflow velocity and pressure distributions of the model with the mesh size 0.4. The figure shows the distributions when the ball was located at x = 0m, x = 0.025m, and x = 0.05m. The ball moved 0.025m within 0.00227s

and moved 0.05m within 0.00246s. On the velocity distribution of mesh size 0.6 and mesh size 0.4 showed a clear shock wave at the entrance of the pipe. However, the model with the smaller mesh size shows reduction in the amount of the air pass through the gap between the ball and the pipe wall. The high pressure region was shown at the entrance of the pipe and the front surface of the ball on the pressure distribution of both mesh size.

Mesh size 0.2

Figure 4.23 shows the airflow velocity and pressure distributions of the model with the mesh size 0.2. The figure shows the distributions when the ball was located at x = 0m, x = 0.025m, and x = 0.05m. The ball moved 0.025m within 0.00317s and moved 0.05m within 0.00336s. The velocity distribution of mesh size 0.2 shows a clear shock wave at the entrance of the pipe. However, only a little amount of the air passes around the ball when the ball located at x=0.05m. An irregular shape was observed on the pressure distribution compared to the velocity profile.

4.3.2 Velocity Profile of the Modified Model

Ball Velocity - Displacement Response

Figure 4.24 shows the ball velocity – displacement responses predicted using the analytical models with different mesh sizes. The analytically predicted responses appear to be close to each other for various mesh sizes except mesh size 0.2. The velocity of mesh size 0.2 converges faster than other velocity plots. Table 4.7 presents analytically predicted ball velocity at x = 0.025m and 0.05m for different mesh sizes. The predicted ball velocity varies from 83.4149m/s to 102.16m/s at x = 0.025m and varies 128.651m/s

to 165.18m/s at x = 0.005m. As the mesh size gets finer, the predicted ball velocity appears to increases at a given location at x=0.025m. However, it appears that there is no tendency at a given location at x=0.05m.

Ball Velocity – Time Response

Figure 4.25 shows the analytically predicted ball velocity – time responses for different mesh sizes. As shown, the ball velocity increases as time elapses in general. Table 4.8 presents analytically predicted ball velocity at the elapsed time t = 0.001sec. and t = 0.002sec. for different mesh sizes. As presented in the table, the predicted ball velocity appears to decrease at a given time as the mesh size gets finer.

Displacement – Time Response

Figure 4.26 shows the analytically predicted ball displacement – time responses for different mesh sizes. The elapsed time at x = 0.05 m was 0.00224 sec. for the mesh size 1, 0.00231 sec. for the mesh size 0.8, 0.00239 sec. for the mesh size 0.6, 0.00246 sec. for the mesh size 0.4, 0.00336 sec. for the mesh size 0.2. Table 4.9 presents analytically predicted ball displacement at the elapsed time t = 0.0015sec. and t = 0.0025sec. for different mesh sizes. As the mesh size gets finer, the predicted ball displacement appears to decrease at a given time in general.

4.4 Verification on the Velocity Profile of the Basic Model

As mentioned in Section 1.3, only the analytically predicted ball velocity profile of the basic model was verified with theoretical approximation. The analytically predicted profile was averaged since no clear influence of the mesh size was identified.

4.4.1 Basic Model

Equations of the Theoretical Approximation-Basic Model

The basic model properties are

P_0 *: 1atm*

ρ : 1.225 kg/m^3

A *:* $1.13 \times 10^{-3} m^2$

m : $2.7 \times 10^{-3} kg$

where, P_0 is the initial pressure, ρ is density of the air A is cross-sectional area of the Ping-Pong ball, and m is the mass of the Ping-Pong ball.

Define the characteristic length of the basic model,

$$\lambda \equiv \frac{m}{\rho A} = 1.95$$

Insert properties and the value of the characteristic length to Equation 3.11. It is possible to obtain the theoretical ball velocity function of displacement for the basic model as an Equation 4.1.

$$v(x)\_basic = 287.61 \left[\frac{x}{x+1.95} \sqrt{1 + 2\frac{1.95}{x}} \right] \quad (4.1)$$

Also, the theoretical ball velocity function of time for the basic model as Equation 4.2 and the theoretical ball displacement function of time for the basic model as Equation 4.3.

$$v(t) = \frac{287.61}{\sqrt{1+\frac{1.95}{42410t^2}}} \tag{4.2}$$

$$x(t) = 287.61\left[\sqrt{1+\frac{42410t^2}{1.95}} - 1\right] \tag{4.3}$$

Ball Velocity - Displacement Verification

Figure 4.27 shows the theoretically approximated ball velocity – displacement response. It is shown by a black solid line. The averaged analytically predicted response is also shown with a black dotted line in the figure. As shown in the figure, the theoretical approximated ball velocity is slightly greater than the analytically predicted ball velocity. However, the theoretically approximated response is very close to the averaged analytically predicted response overall.

Ball Velocity - Time Verification

Figure 4.28 shows both the theoretically approximated and analytically predicted ball velocity – time response. The theoretically approximated response is shown as a solid black line and the analytically predicted response is shown as a dotted black line. The theoretically approximated response shows a linear response. However, the averaged analytically predicted response show some fluctuations. The time gap is observed between the two responses. The reason of the time gap is that in the theoretical scenario, the ball sits right front of the entrance, but in the case of the analytical model, the ball sits 10 mm offset from the entrance.

Ball Displacement - Time Verification

Figure 4.29 shows the theoretically approximated ball displacement – time response. The response is compared with the analytically predicted response in the figure. The theoretically approximated response is shown in a solid black line and the analytically predicted response is shown in a dotted black line. As shown in the figure, the theoretically approximated ball displacement – time response has somewhat similar tendency to the analytically predicted response. However, the theoretically approximated response appears to be shifted more away from the inlet.

4.4.2 Basic_2 Model

Equations of the Theoretical Approximation-Basic_2 Model

The basic_2 model properties are

P_0 *: 4atm*

ρ : 4.9009 kg/m^3

A *:* $1.13 \times 10^{-3} m^2$

m : $2.7 \times 10^{-3} kg$

where, P_0 is the initial pressure, ρ is density of the air A is cross-sectional area of the Ping-Pong ball, and m is the mass of the Ping-Pong ball.

Define the characteristic length of the basic model,

$$\lambda \equiv \frac{m}{\rho A} = 0.451$$

Insert properties and the value of the characteristic length to Equation 3.11. It is possible to obtain the theoretical ball velocity function of displacement for the basic model as an Equation 4.4.

$$v(x)\_basic = 287.61\left[\frac{x}{x+0.451}\sqrt{1+2\frac{0.451}{x}}\right] \tag{4.4}$$

Also, the theoretical ball velocity function of time for the basic model as Equation 4.5 and the theoretical ball displacement function of time for the basic model as Equation 4.6.

$$v(t) = \frac{287.61}{\sqrt{1+\frac{0.451}{183200t^2}}} \tag{4.5}$$

$$x(t) = 287.61\left[\sqrt{1+\frac{183200t^2}{0.451}}-1\right] \tag{4.6}$$

Ball Velocity - Displacement Verification

Figure 4.30 shows the theoretically approximated ball velocity – displacement response. It is shown in a black solid line. The averaged analytically predicted response is also shown with a black dotted line in the figure. As shown in the figure, the theoretical approximated ball velocity is slightly greater than the analytically predicted ball velocity.

Ball Velocity - Time Verification

Figure 4.31 shows both the theoretically approximated and analytically predicted ball velocity – time response. The theoretically approximated response is shown in a solid black line and the analytically predicted response is shown in a dotted black line.

Ball Displacement - Time Verification

Figure 4.32 shows the theoretically approximated ball displacement – time response. The response is compared with the analytically predicted response in the figure. The theoretically approximated response is shown in a solid black line and the analytically predicted response is shown in a dotted black line. As shown in the figure, the theoretically approximated ball displacement – time response has somewhat similar tendency to the analytically predicted response. However, the theoretically approximated response appears to be shifted more away from the inlet.

Table 4.1 Predicted ball velocity at x = 0.025m, 0.05m for different mesh sizes (Basic model)

Mesh size	Ball velocity, m/s	
	x = 0.025 m	x = 0.05 m
1.0	60.8577	84.0754
0.8	41.3947	60.867
0.6	25.7804	28.9388
0.4	30.6974	36.6035
0.2	69.9296	77.9121

Table 4.2 Predicted ball velocity at time t=0.001sec., t=0.002sec for different mesh sizes (Basic model)

Mesh size	Ball velocity, m/s	
	t = 0.001 sec.	t = 0.002 sec.
1.0	7.2832	75.962
0.8	13.416	49.7824
0.6	2.2790	13.6134
0.4	8.5864	29.2798
0.2	12.6014	78.5408

Table 4.3 Predicted ball location at time t=0.001sec., t=0.002sec for different mesh sizes (Basic model)

Mesh size	Displacement, m	
	t = 0.001 sec.	t = 0.002 sec.
1.0	0.002	0.041
0.8	0.004	0.034
0.6	0.001	0.007
0.4	0.003	0.020
0.2	0.003	0.060

Table 4.4 Predicted ball velocity at x = 0.025m, 0.05m for different mesh sizes (Basic_2 model)

Mesh size	Ball velocity, m/s	
	x = 0.025 m	x = 0.05 m
1.0	40.0112	107.155
0.8	29.1244	36.9561
0.6	93.9353	134.808
0.4	97.7851	133.993
0.2	104.938	117.109

Table 4.5 Predicted ball velocity at time *t*=0.001sec., *t*=0.002sec for different mesh sizes (Basic_2 model)

Mesh size	Ball velocity, m/s	
	t = 0.001 sec.	*t* = 0.002 sec.
1.0	14.1597	71.0581
0.8	12.1122	30.8572
0.6	116.248	153.422
0.4	128.337	140.069
0.2	116.432	118.433(*t=0.0015*)

Table 4.6 Predicted ball location at time *t*=0.001sec., *t*=0.002sec for different mesh sizes (Basic_2 model)

Mesh size	Displacement, m	
	t = 0.001 sec.	*t* = 0.002 sec.
1.0	0.004	0.037
0.8	0.005	0.028
0.6	0.037	0.185
0.4	0.044	0.183
0.2	0.044	0.103(*t=0.0015*)

Table 4.7 Predicted ball velocity at x = 0.025m, 0.05m for different mesh sizes (Modified model)

Mesh size	Ball velocity, m/s	
	x = 0.025m	x = 0.05m
1.0	83.4149m/s	128.651m/s
0.8	85.9264m/s	165.18m/s
0.6	86.6714m/s	146.197m/s
0.4	102.16m/s	145.476m/s
0.2	113.306m/s	134.786m/s

Table 4.8 Predicted ball velocity at time t=0.0015sec., t=0.0025sec for different mesh sizes (Modified model)

Mesh size	Ball velocity, m/s	
	t = 0.0015 sec.	t = 0.0025 sec.
1.0	15.5609	156.1840
0.8	14.0038	202.6600
0.6	11.704	149.7630
0.4	6.1006	147.4380
0.2	0	2.2599

Table 4.9 Predicted ball location at time t = 0.0015sec., t = 0.0025sec for different mesh sizes (Modified model)

Mesh size	Displacement, m	
	t = 0.0015 sec.	t = 0.0025 sec.
1.0	0.0057	0.0884
0.8	0.0029	0.0863
0.6	0.0028	0.0658
0.4	0.0007	0.0559
0.2	0.0000	0.0002

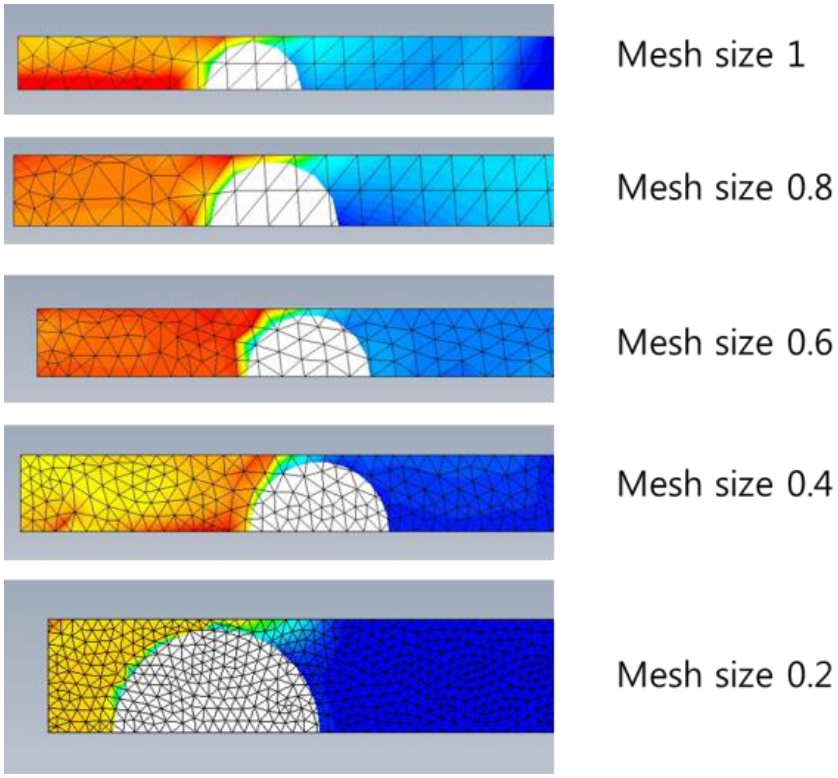

Figure 4.1 Five different mesh sizes (Basic model)

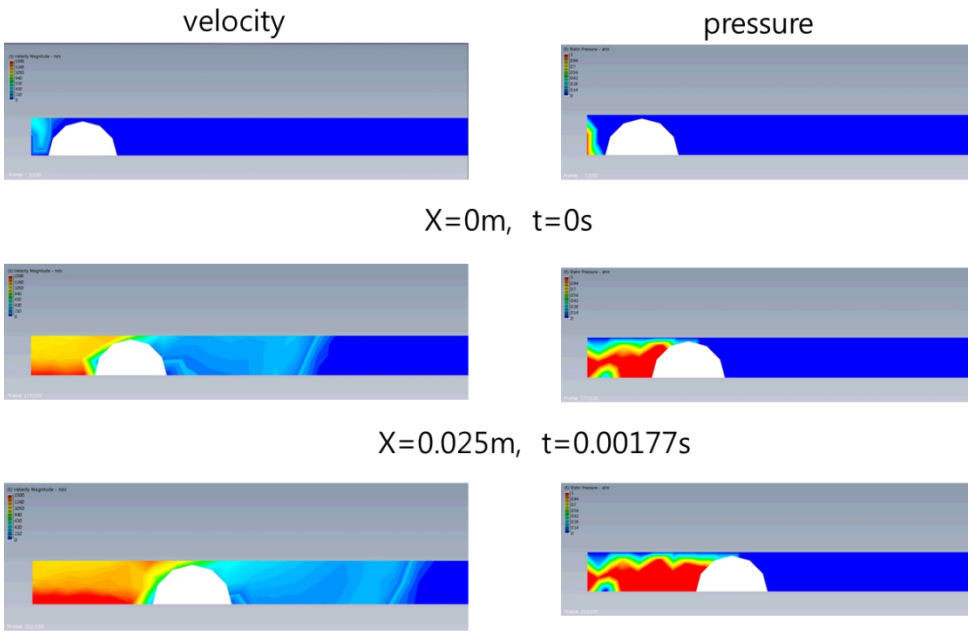

Figure 4.2 Airflow distribution of mesh size 1 (Basic model)

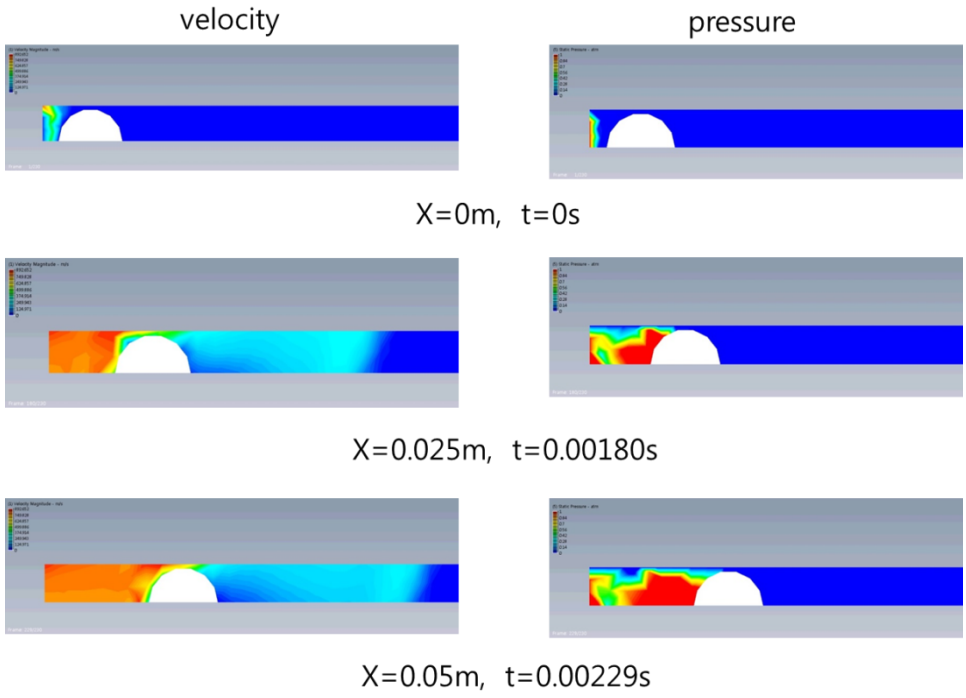

Figure 4.3 Airflow distribution of mesh size 0.8 (Basic model)

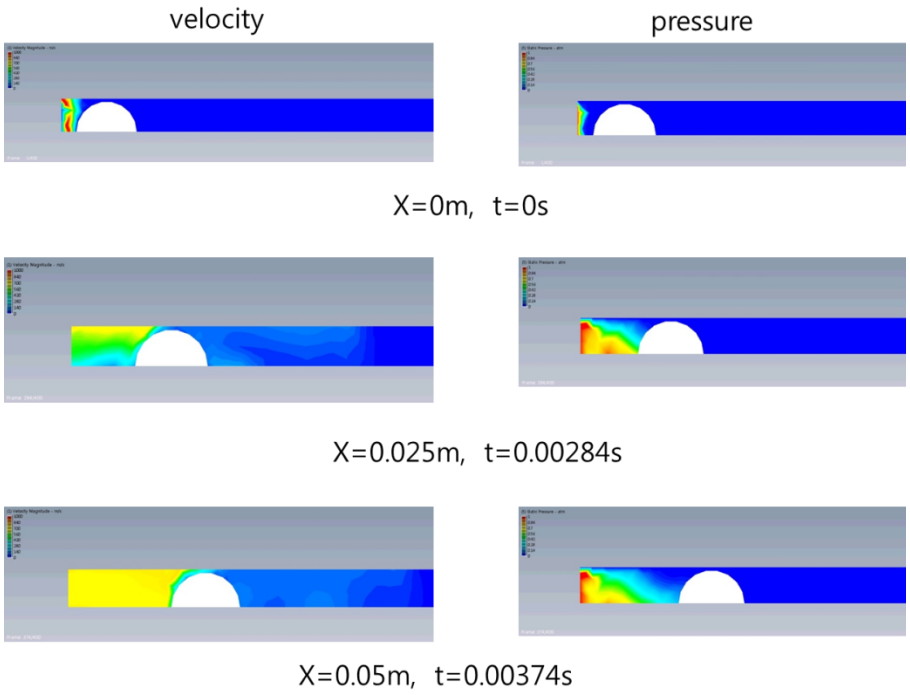

Figure 4.4 Airflow distribution of mesh size 0.6 (Basic model)

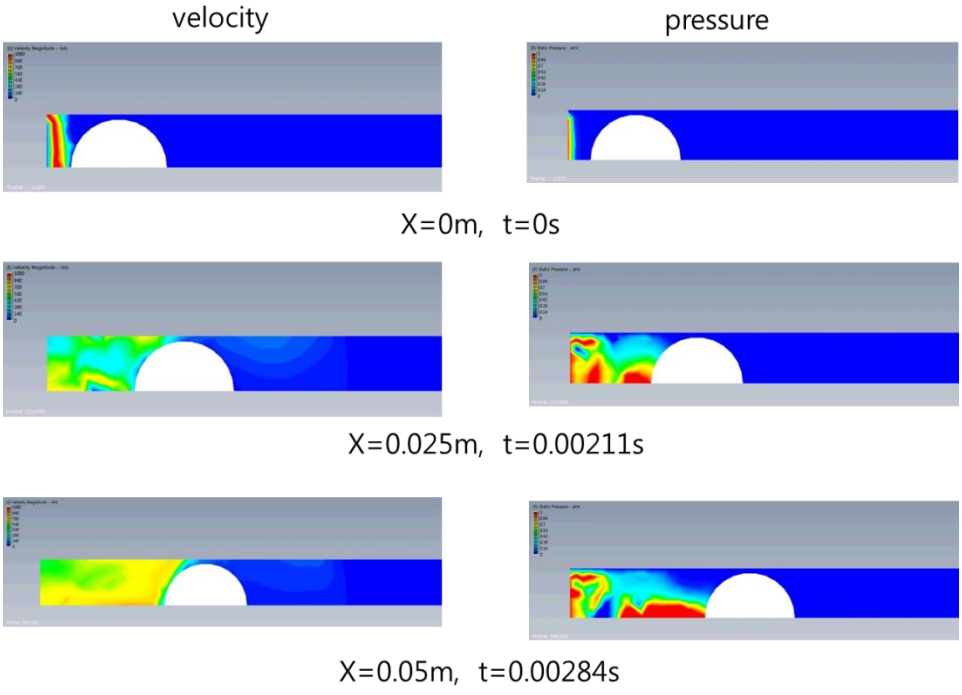

Figure 4.5 Airflow distribution of mesh size 0.4 (Basic model)

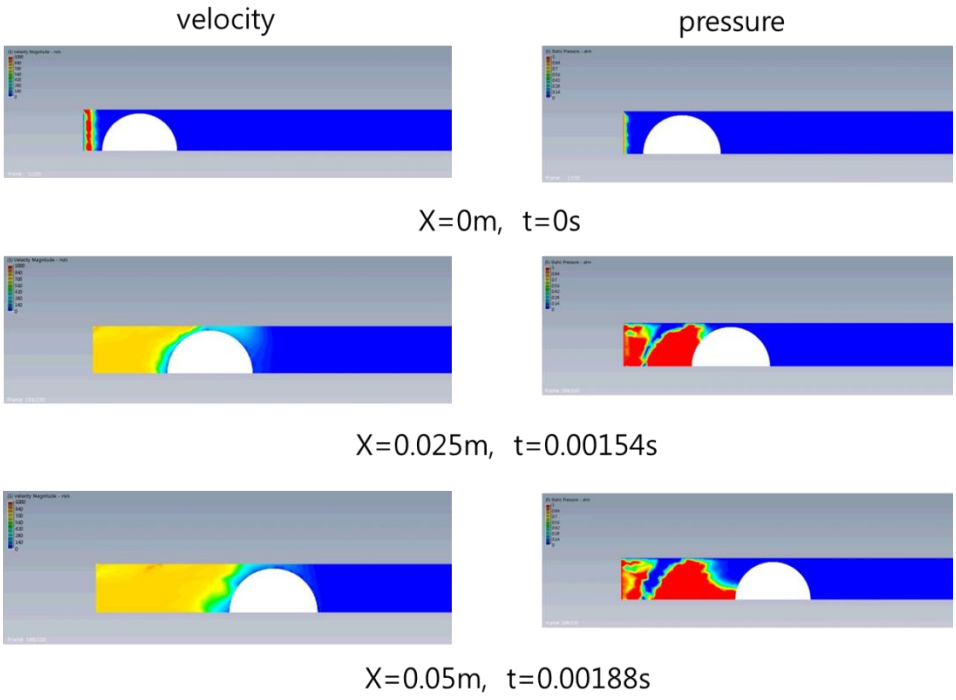

Figure 4.6 Airflow distribution of mesh size 0.2 (Basic model)

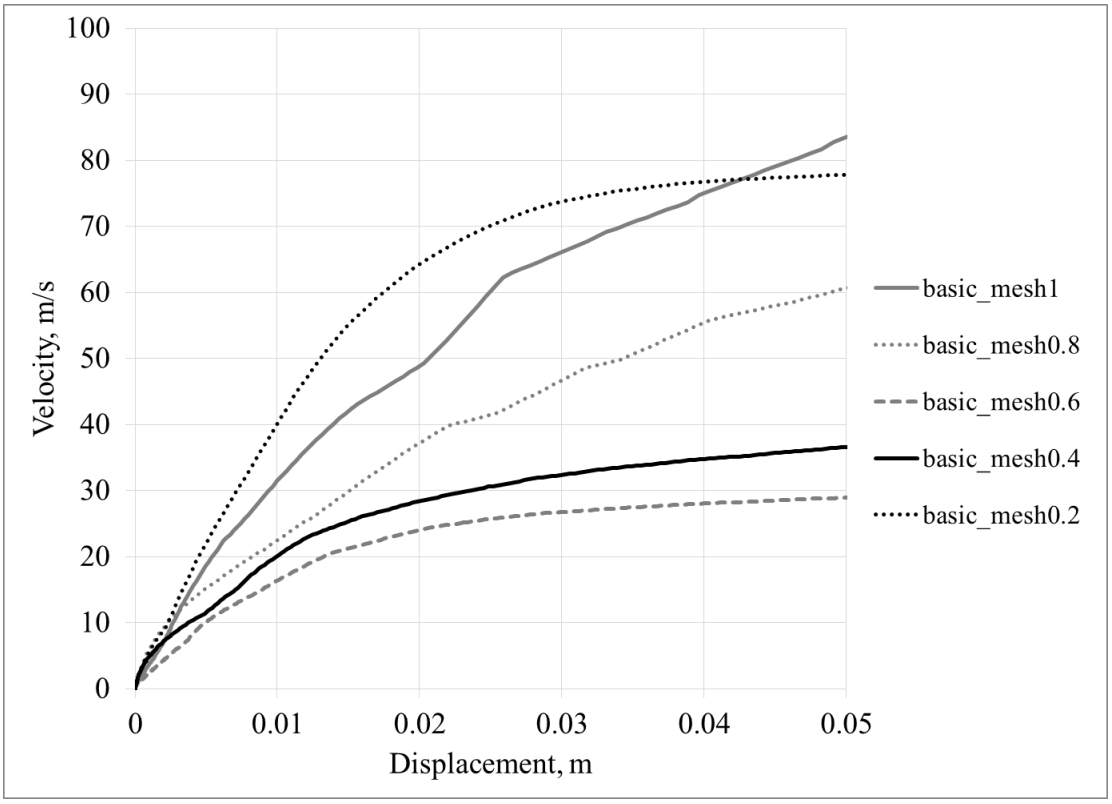

Figure 4.7 The ball velocity - displacement plot of different mesh sizes (Basic model)

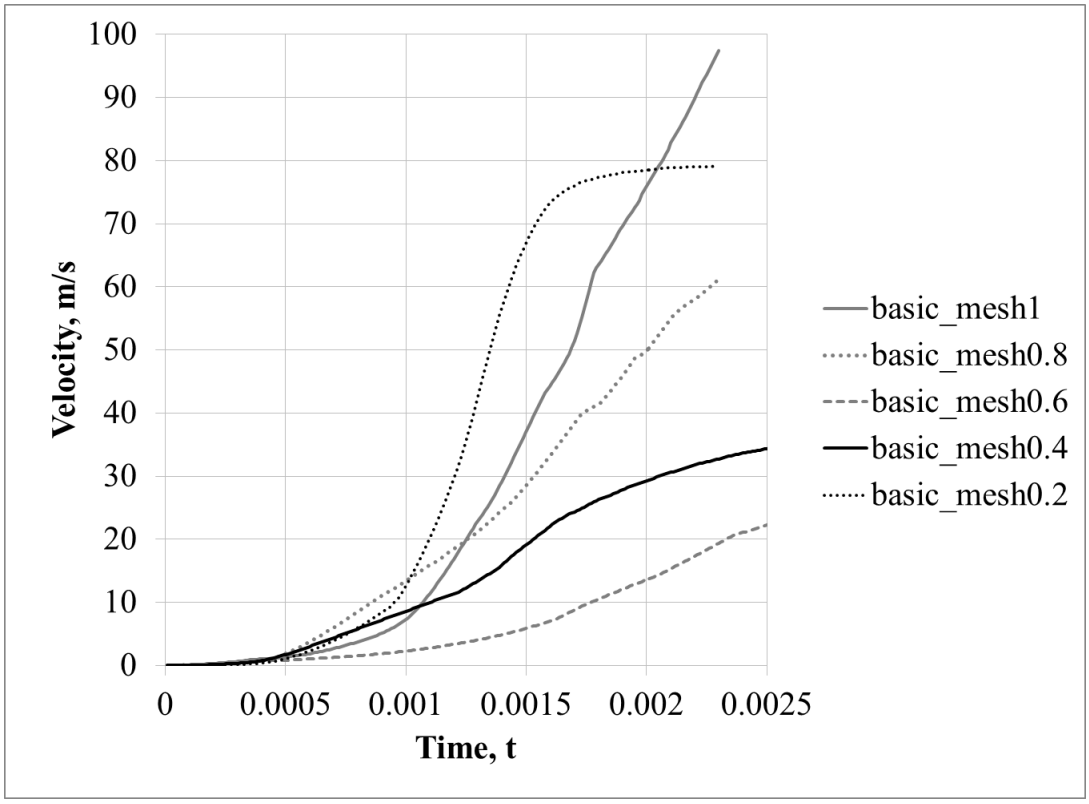

Figure 4.8 The ball velocity - time plot of different mesh sizes (Basic model)

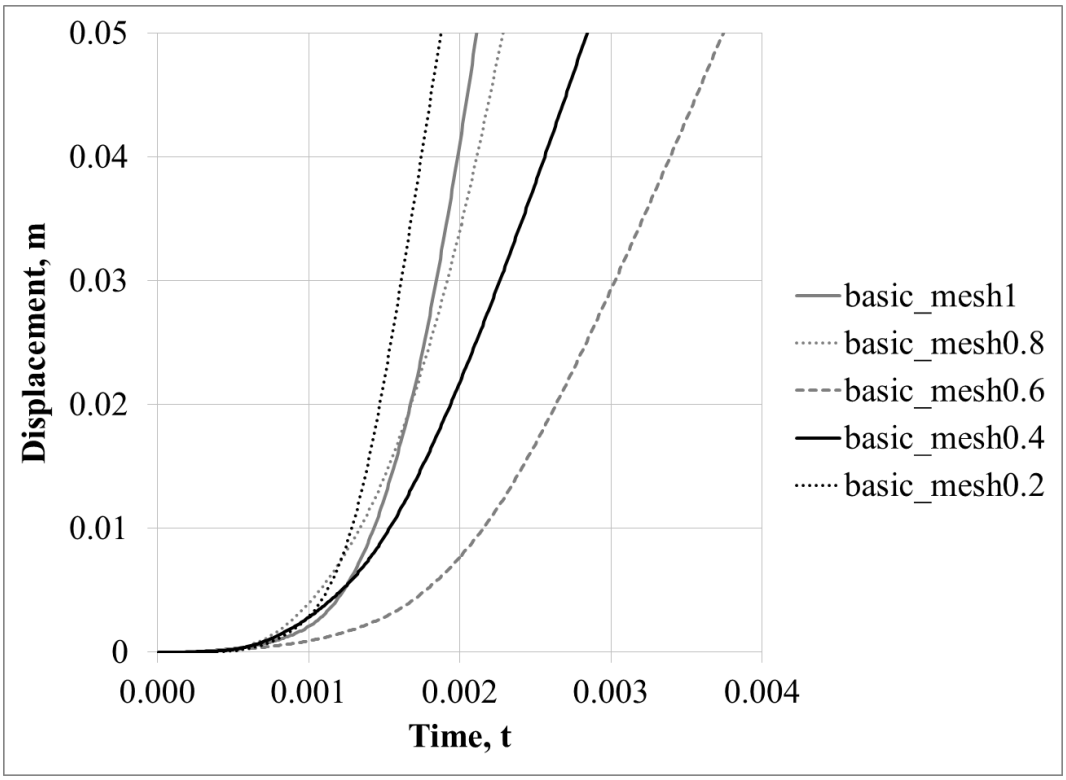

Figure 4.9 The ball displacement - time plot of different mesh sizes (Basic model)

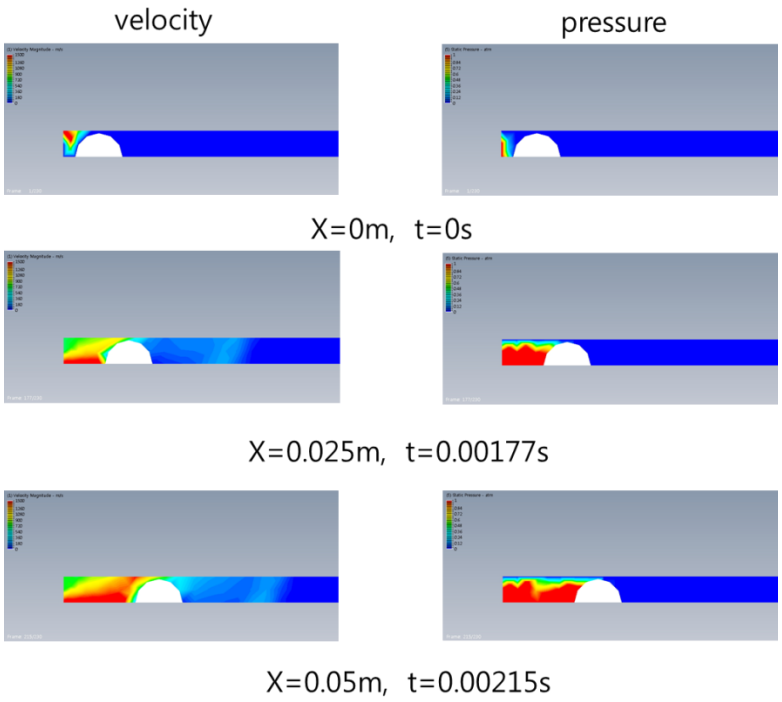

Figure 4.10 Airflow distribution of mesh size 1 (Basic_2 model)

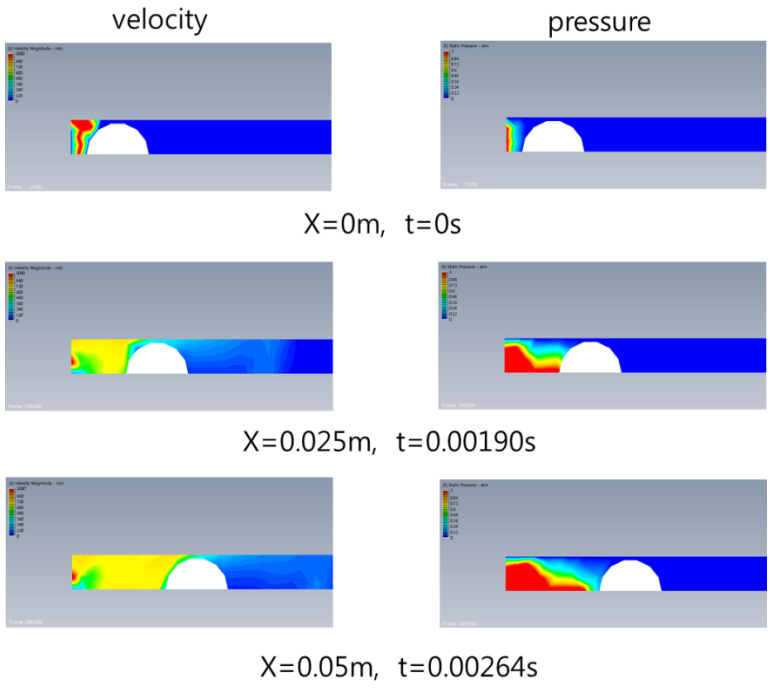

Figure 4.11 Airflow distribution of mesh size 0.8 (Basic_2 model)

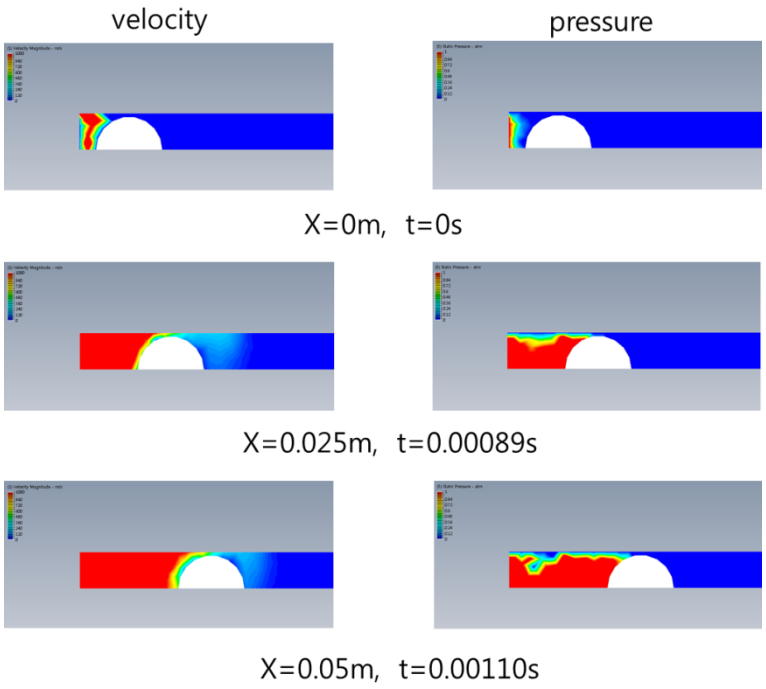

Figure 4.12 Airflow distribution of mesh size 0.6 (Basic_2 model)

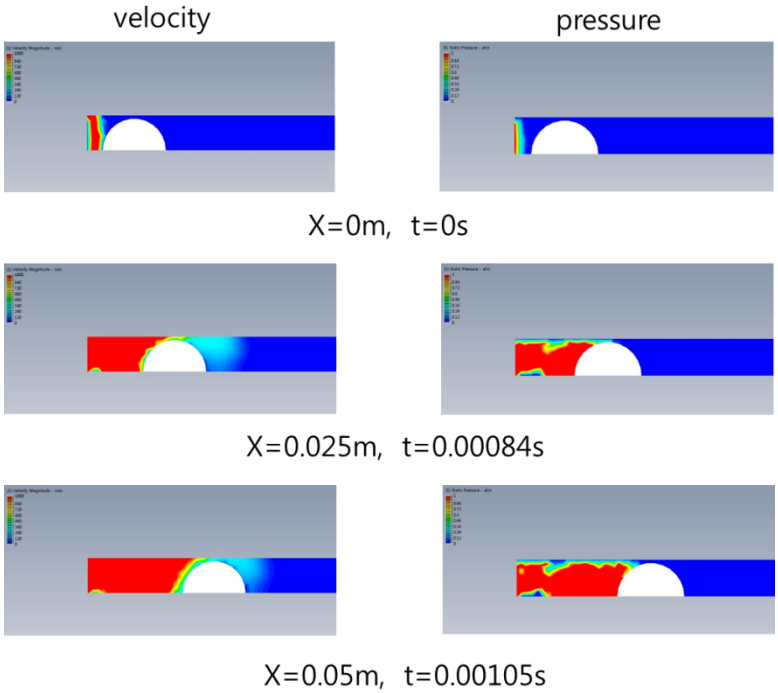

Figure 4.13 Airflow distribution of mesh size 0.4 (Basic_2 model)

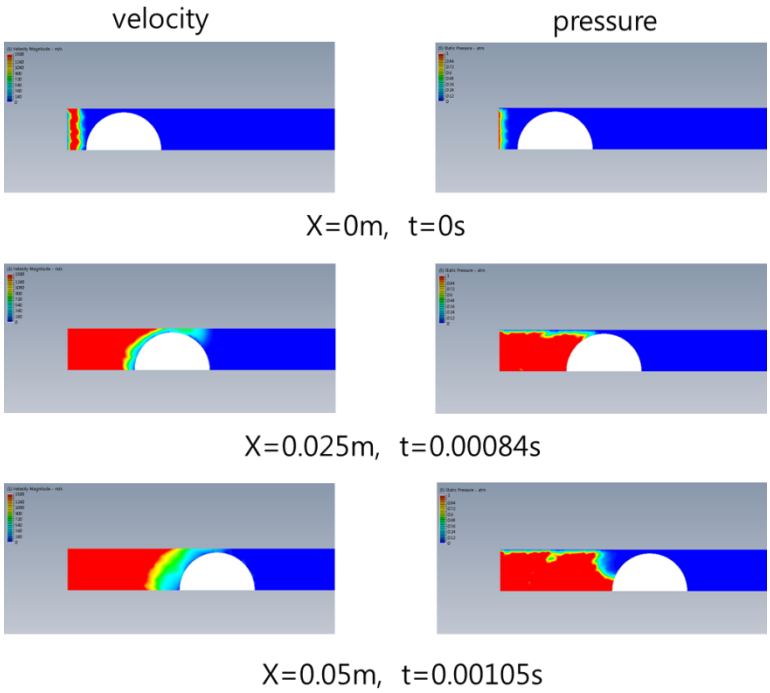

Figure 4.14 Airflow distribution of mesh size 0.2 (Basic_2 model)

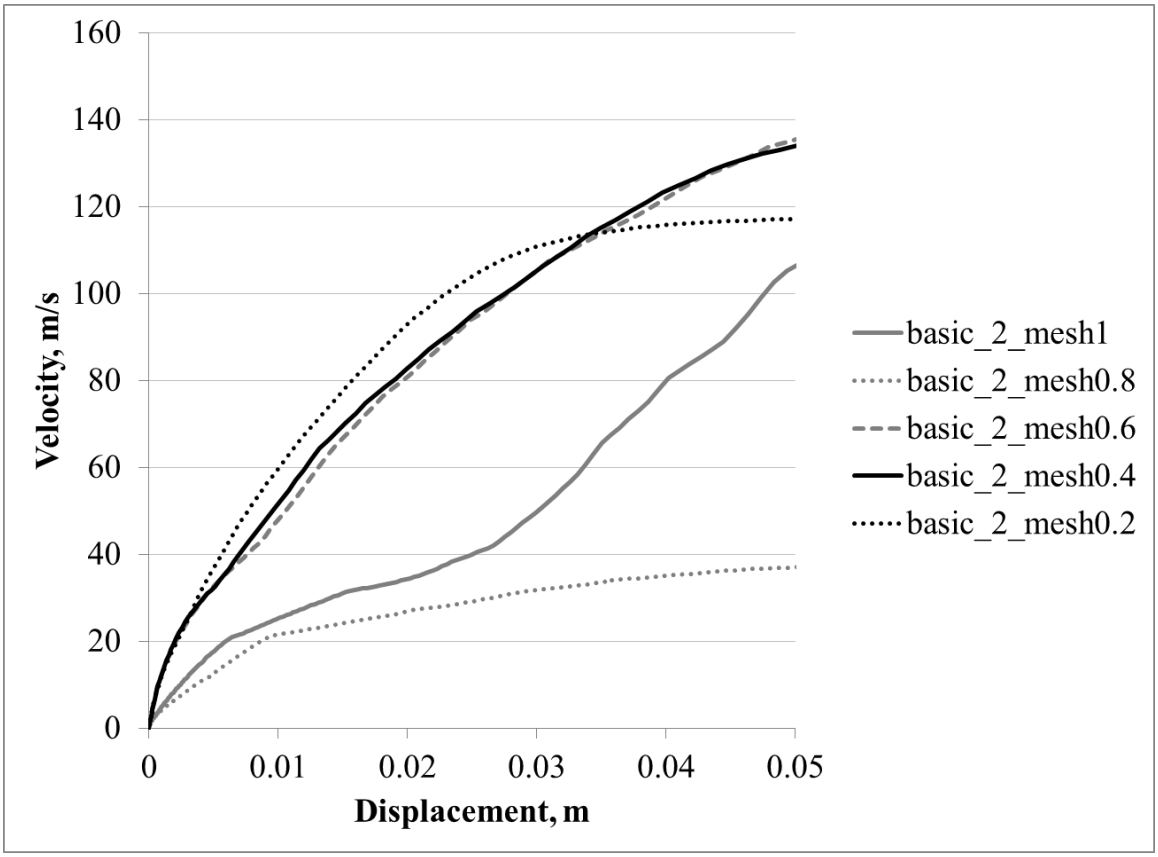

Figure 4.15 The ball velocity - displacement plot of different mesh sizes (Basic_2 model)

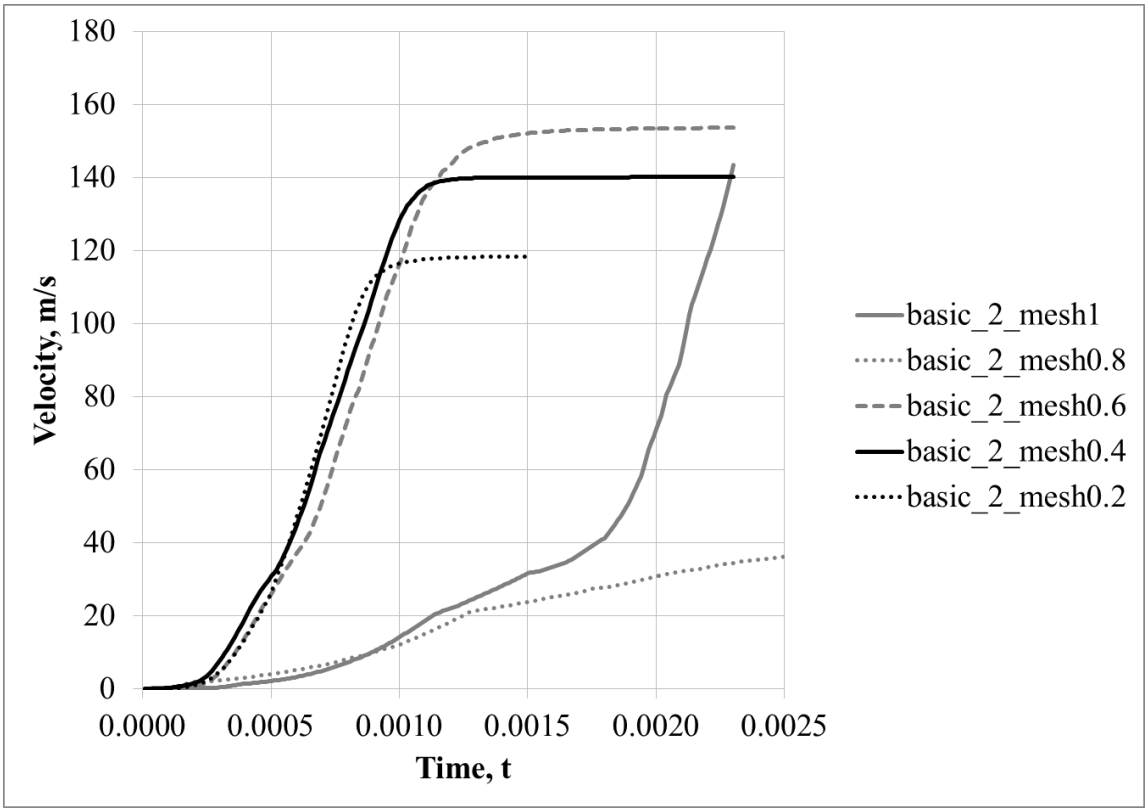

Figure 4.16 The ball velocity - time plot of different mesh sizes (Basic_2 model)

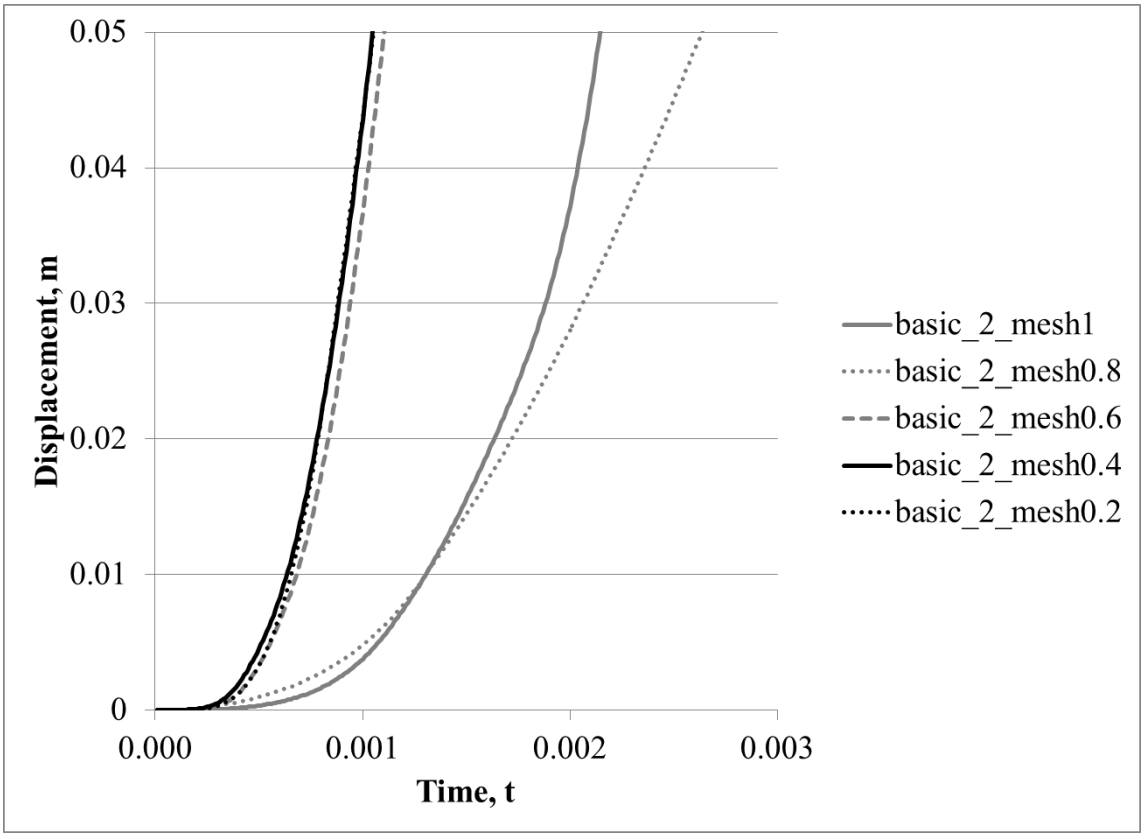

Figure 4.17 The ball displacement - time plot of different mesh sizes (Basic_2 model)

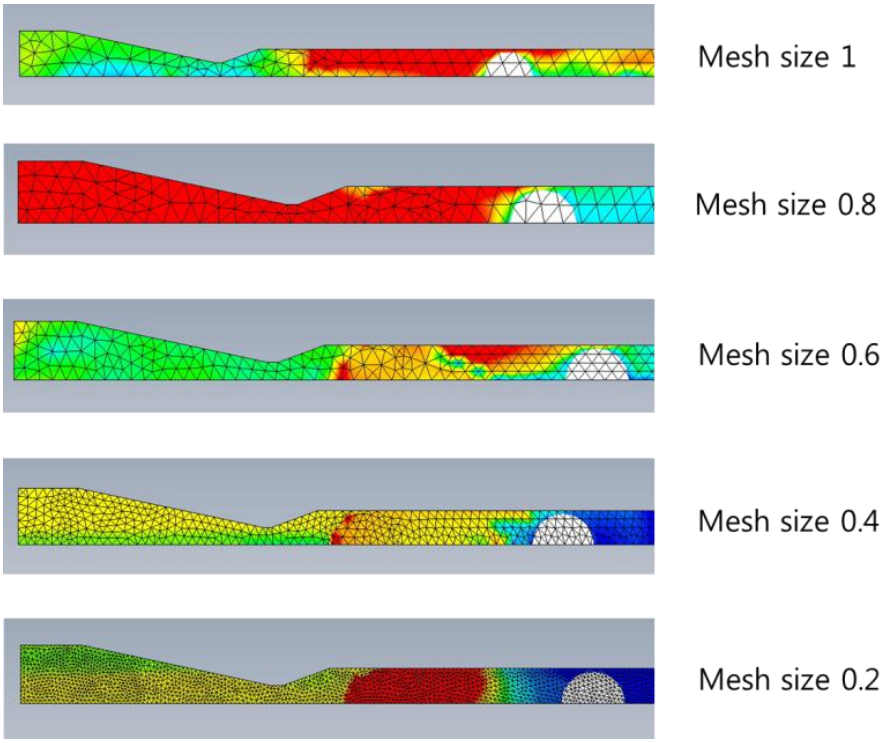

Figure 4.18 Five different mesh sizes (Modified model)

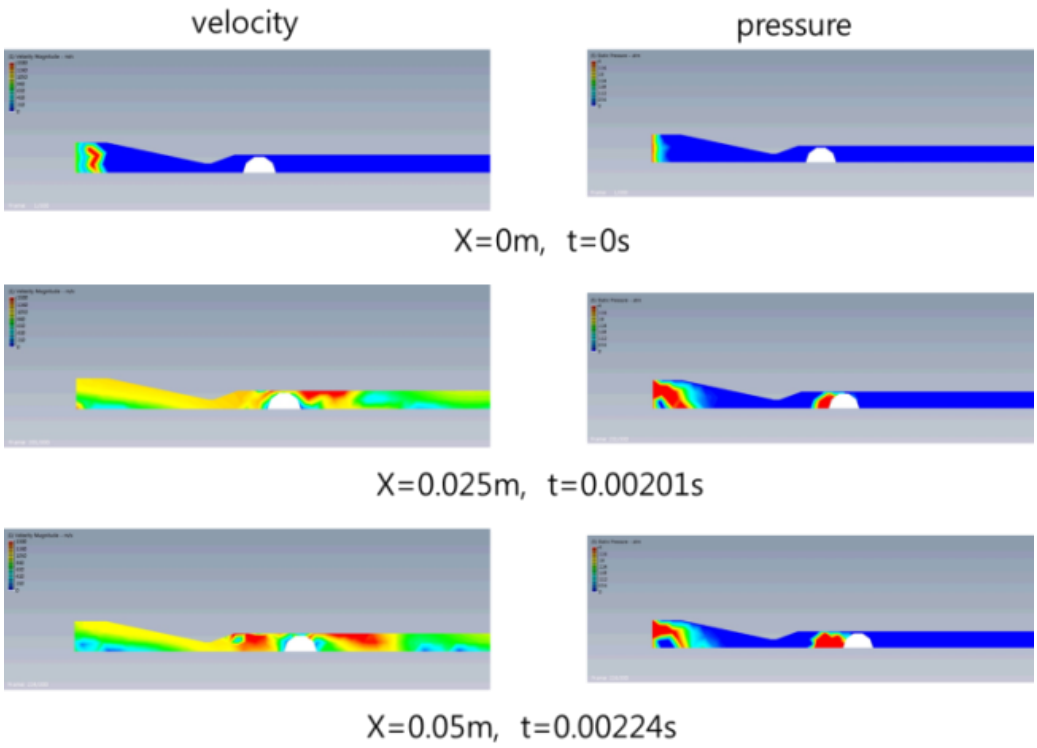

Figure 4.19 Airflow distribution of mesh size 1 (Modified model)

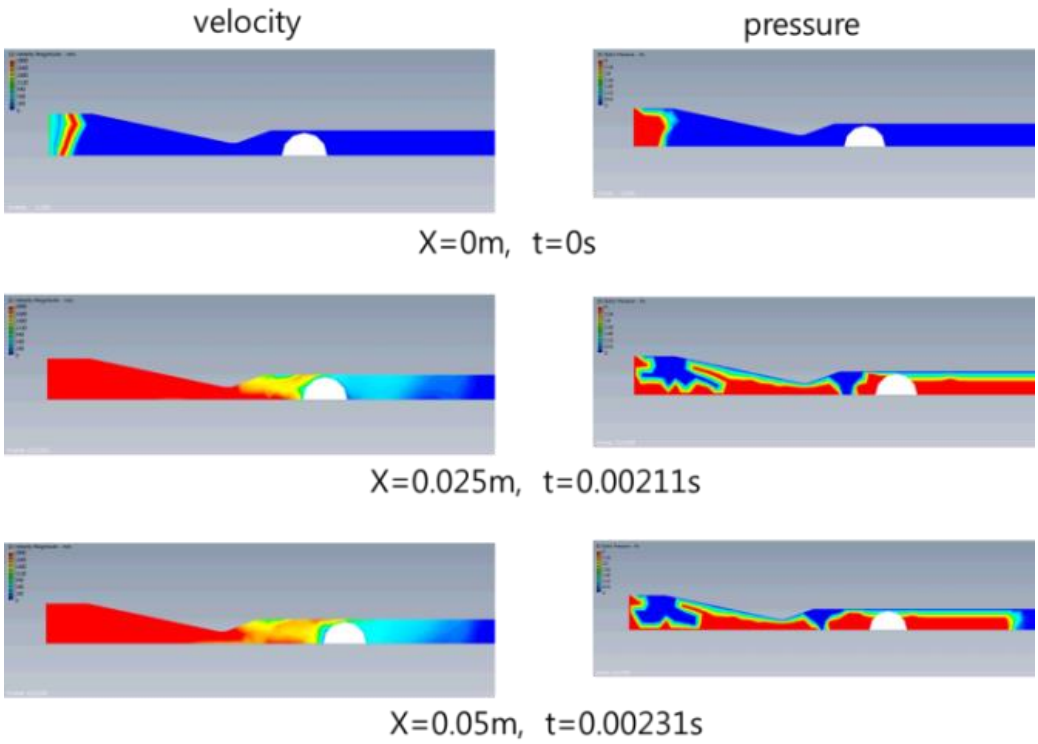

Figure 4.20 Airflow distribution of mesh size 0.8 (Modified model)

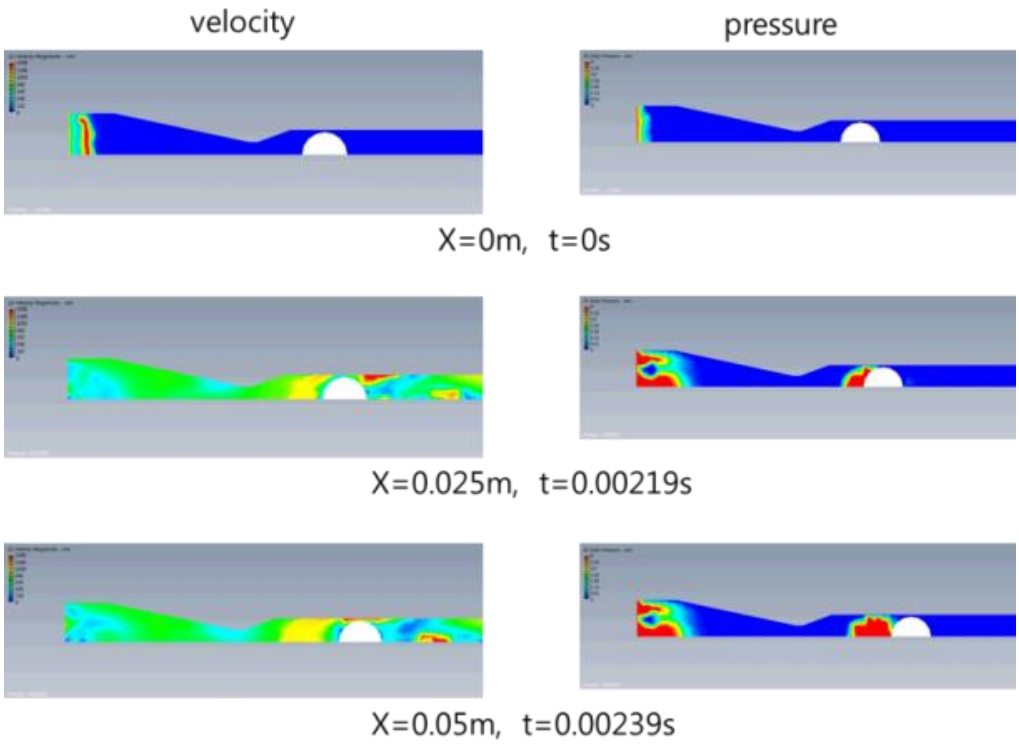

Figure 4.21 Airflow distribution of mesh size 0.6 (Modified model)

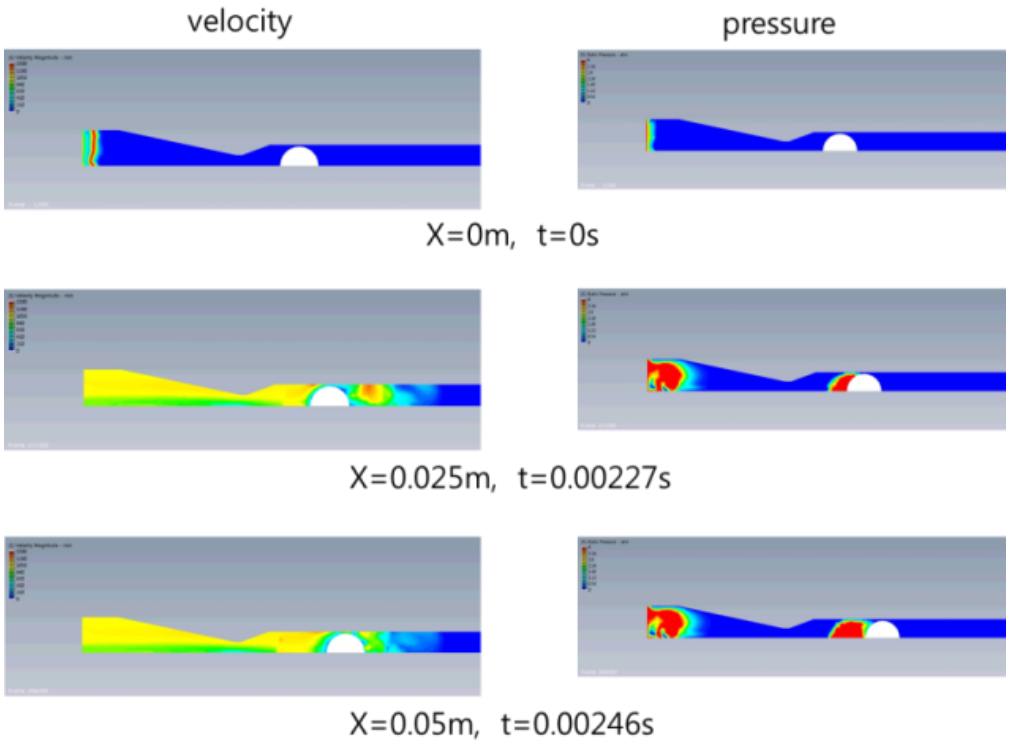

Figure 4.22 Airflow distribution of mesh size 0.4 (Modified model)

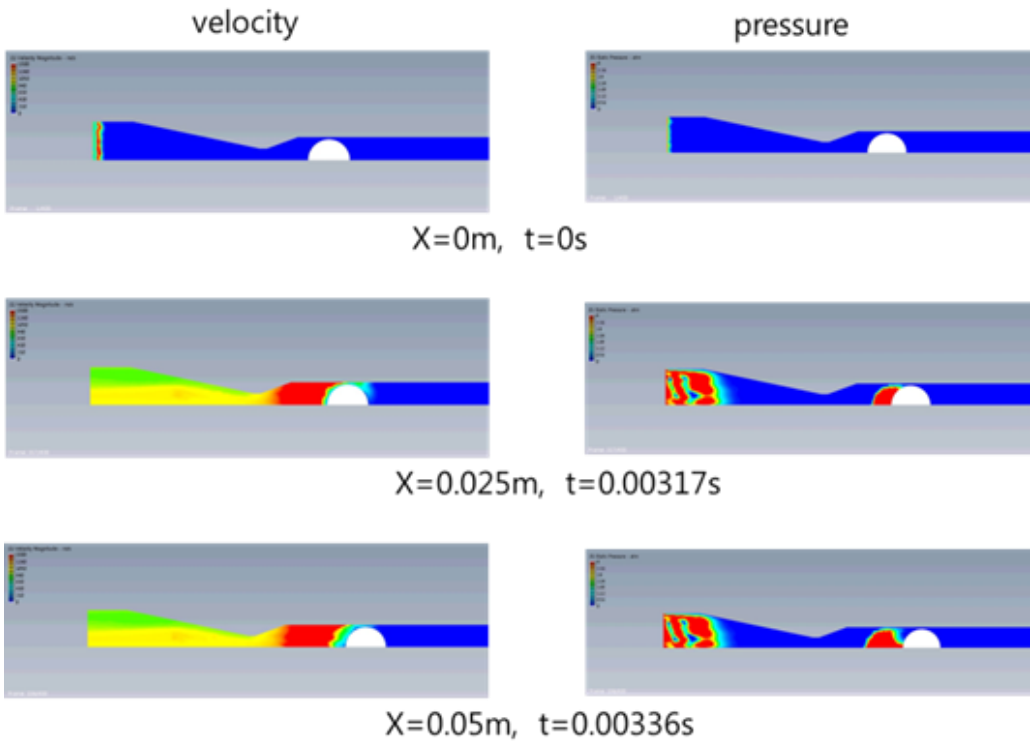

Figure 4.23 Airflow distribution of mesh size 0.2 (Modified model)

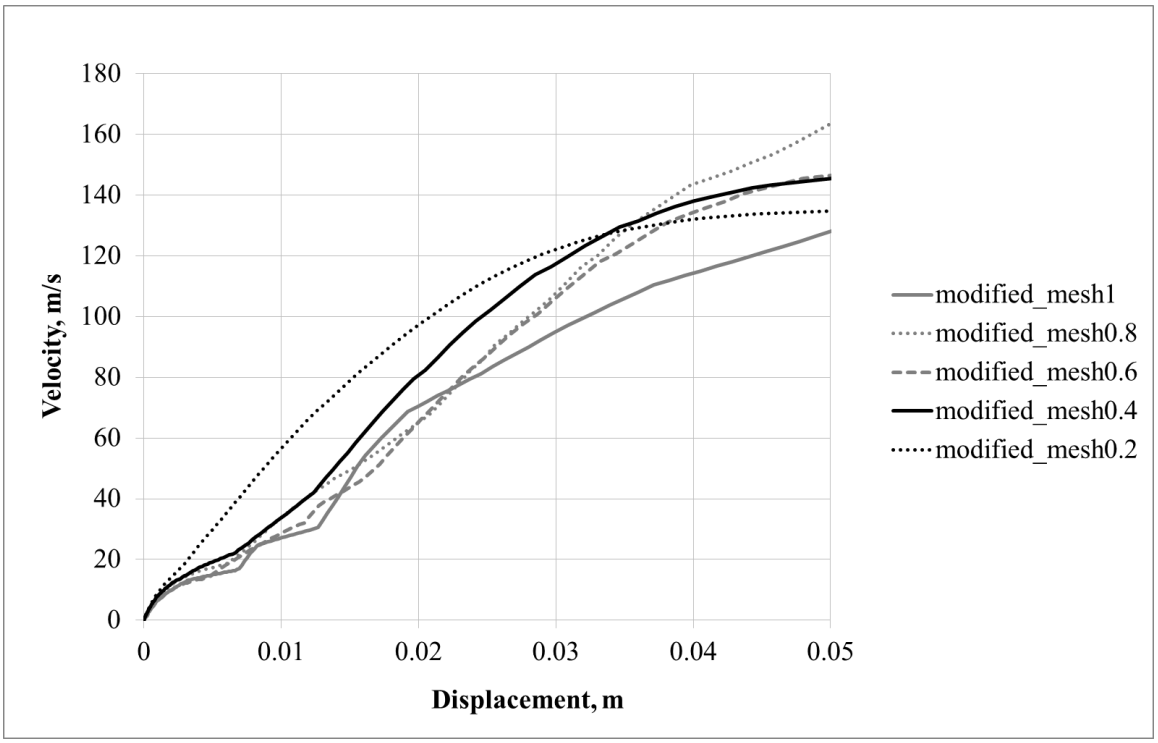

Figure 4.24 The ball velocity - displacement plot of different mesh sizes (Modified model)

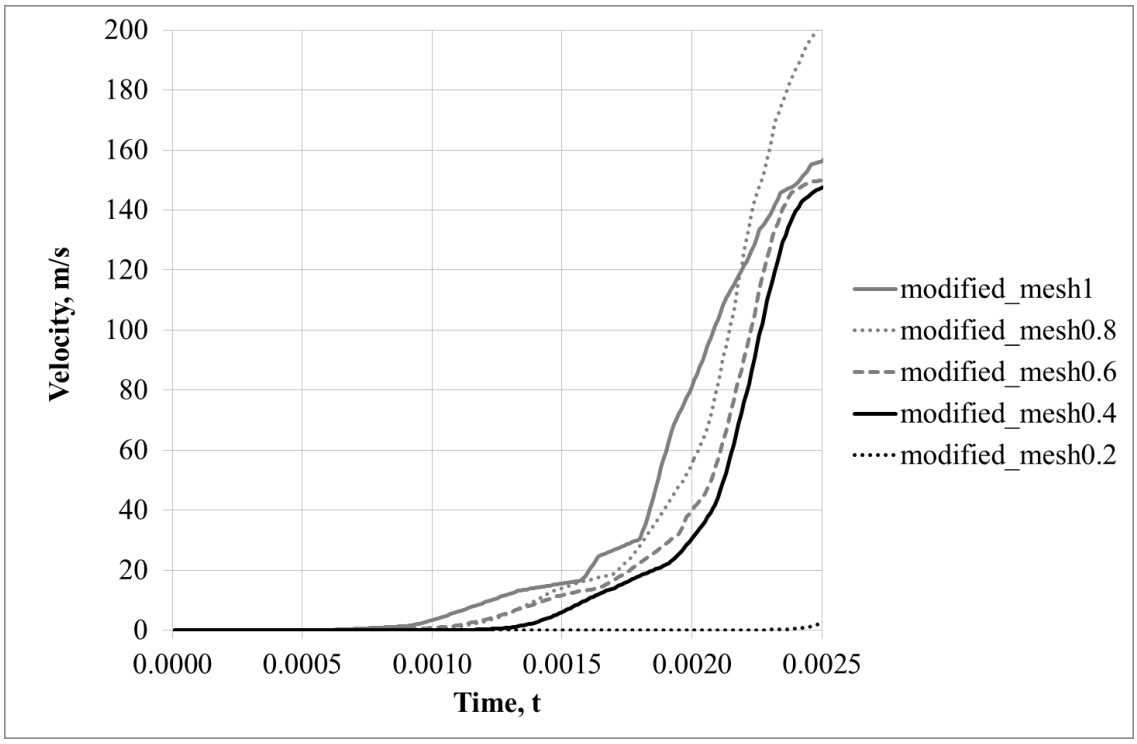

Figure 4.25 The ball velocity - time plot of different mesh sizes (Modified model)

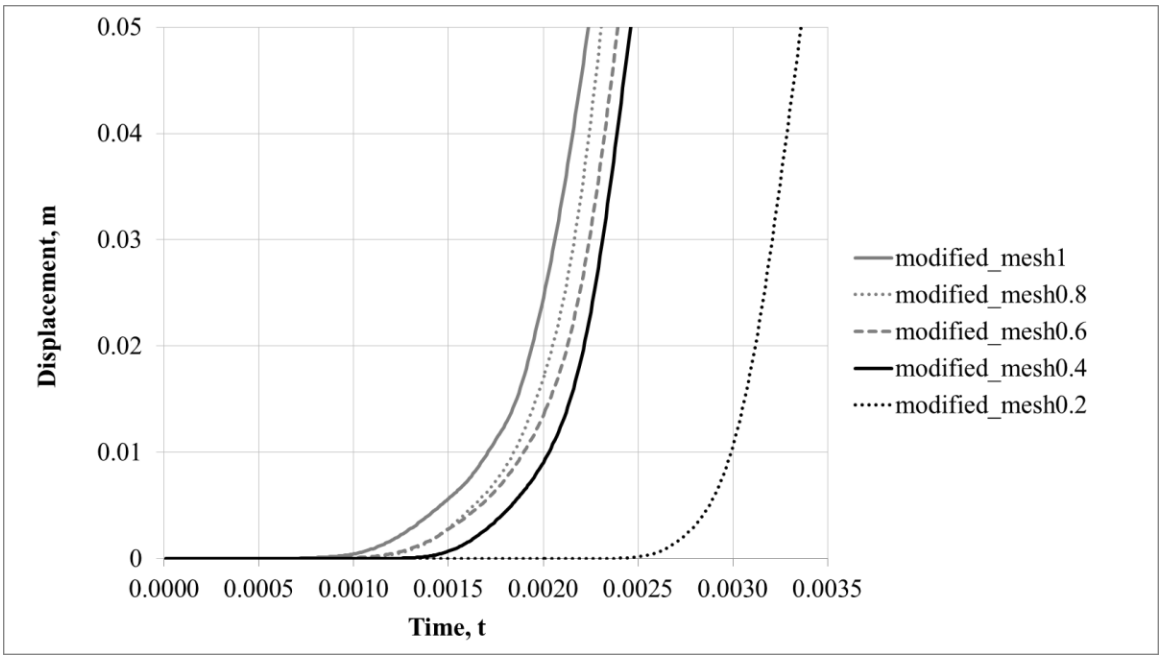

Figure 4.26 The ball displacement - time plot of different mesh sizes (Modified model)

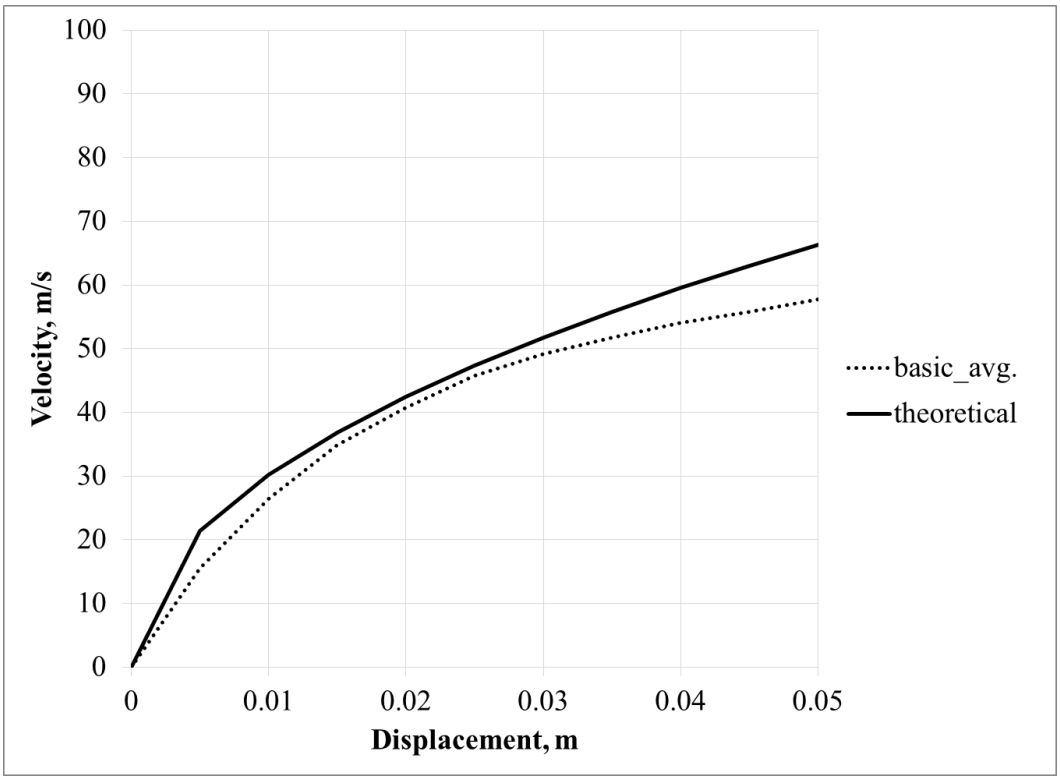

Figure 4.27 The ball velocity - displacement plot of the analytical model and the theoretical approximation (Basic model)

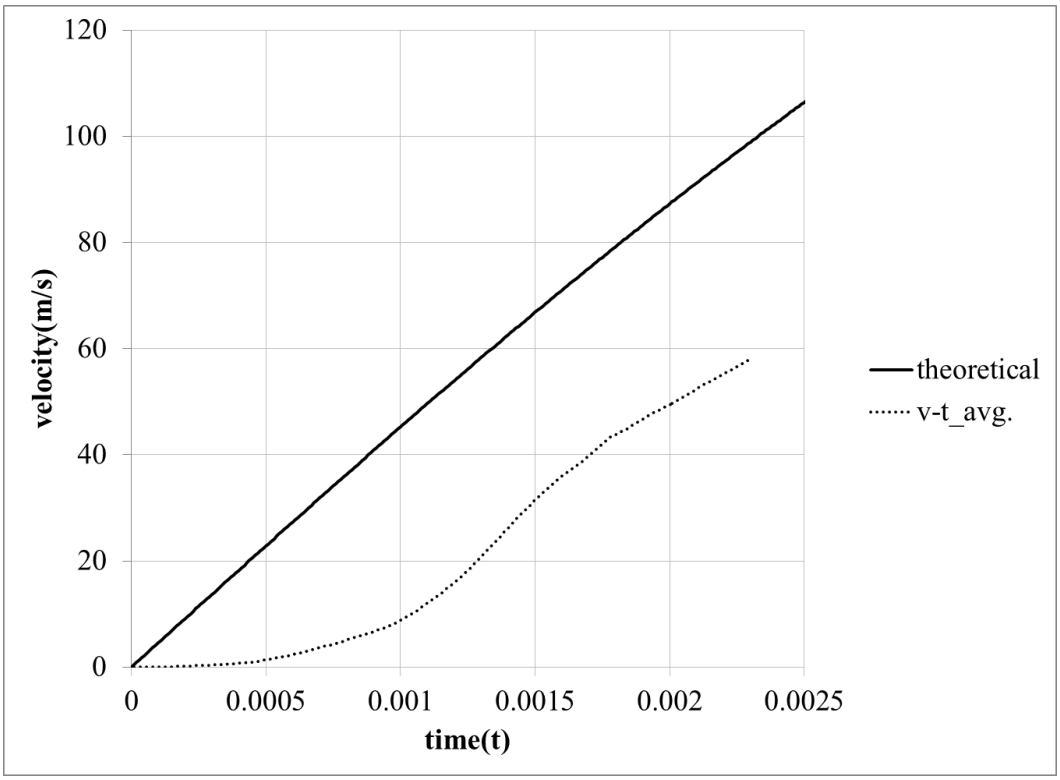

Figure 4.28 The ball velocity - time plot of the analytical model and the theoretical approximation (Basic model)

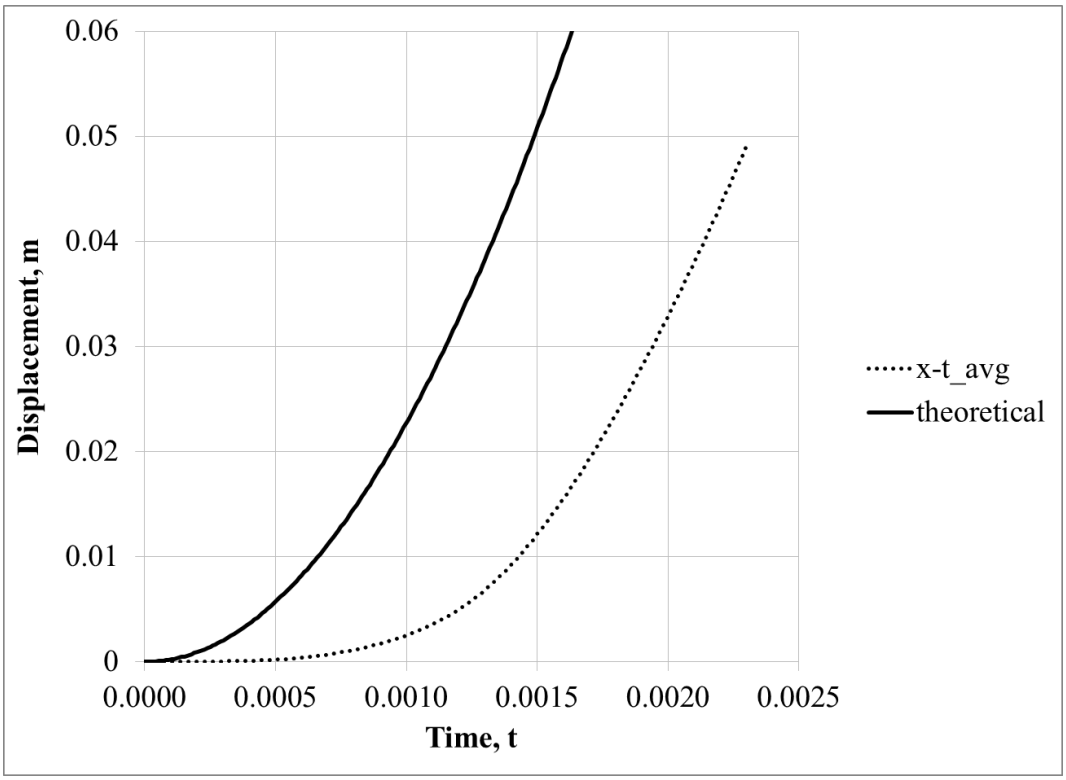

Figure 4.29 The ball displacement - time plot of the analytical model and the theoretical approximation (Basic model)

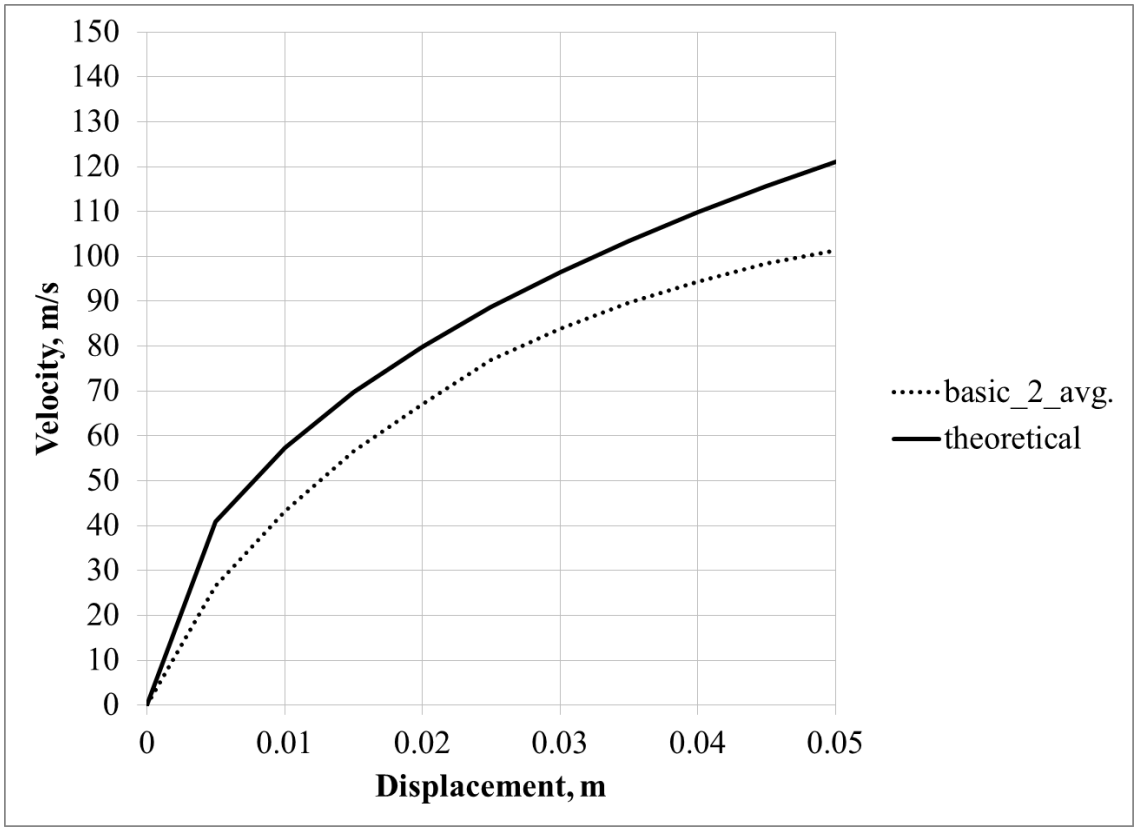

Figure 4.30 The ball velocity - displacement plot of the analytical model and the theoretical approximation (Basic_2 model)

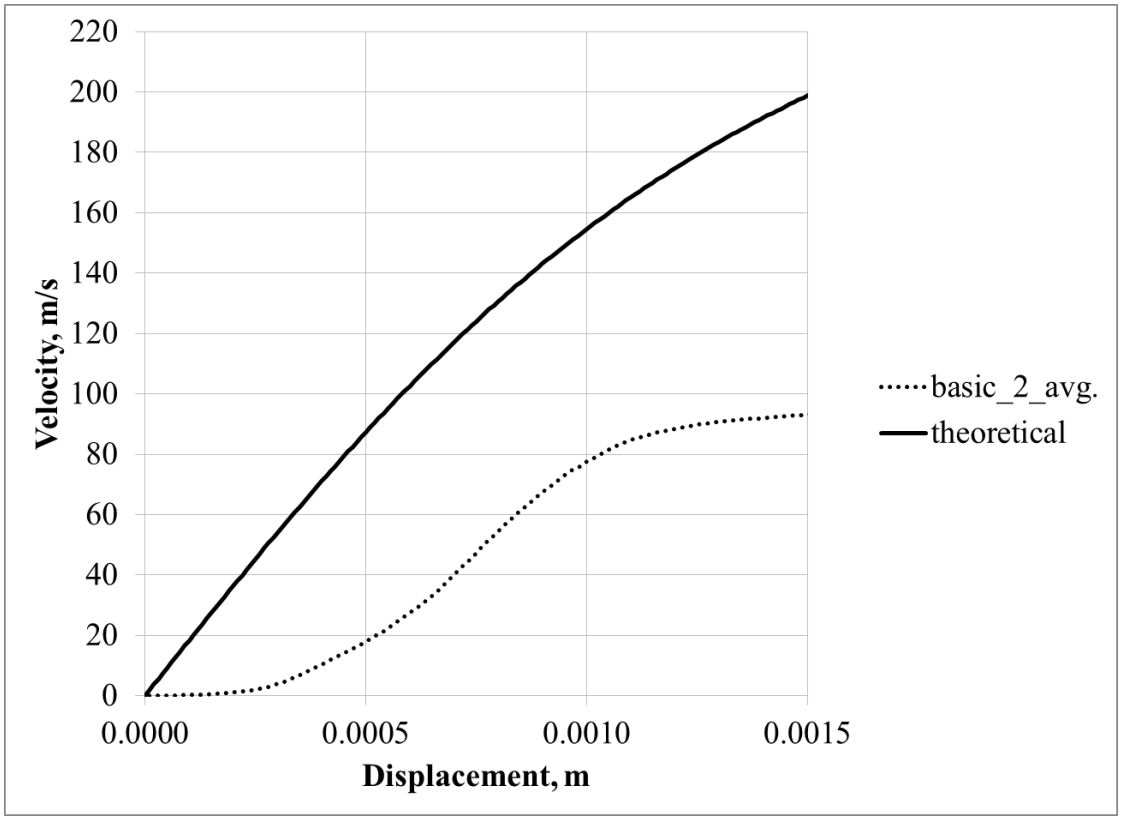

Figure 4.31 The ball velocity - time plot of the analytical model and the theoretical approximation (Basic_2 model)

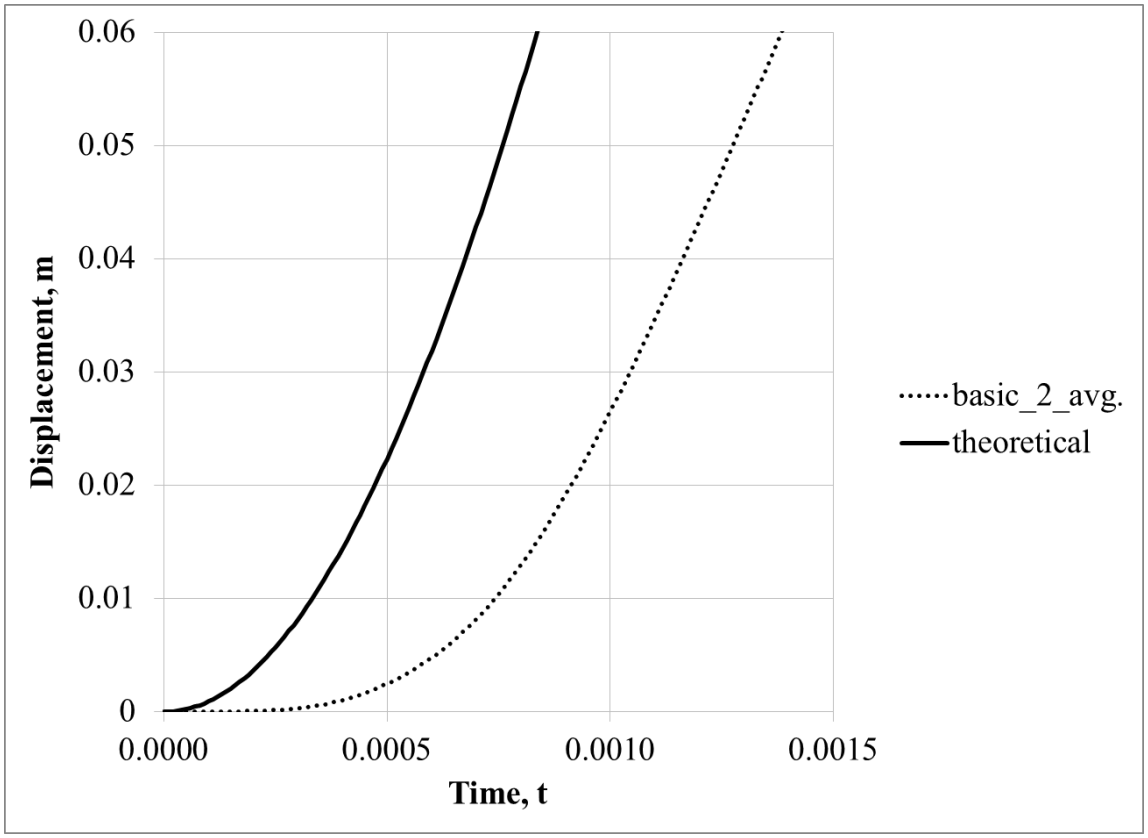

Figure 4.32 The ball displacement - time plot of the analytical model and the theoretical approximation (Basic_2 model)

CHAPTER 5. CONCLUSIONS AND FUTURE WORKS

5.1 Conclusions

Both experimental and analytical studies were previously conducted on a basic Ping-Pong ball gun test. To investigate the fundamental behavior of the gun and to expand knowledge of the fundamental behavior of a modified Ping-Pong ball gun, an analytical study was conducted using commercially available computational fluid dynamics software, 'Autodesk Simulation CFD 2014'.

Analytically predicted ball velocity profiles and airflow distributions for both guns were reviewed. The analytically predicted profiles and distributions were compared with theoretical approximations. However, applying the same theoretical approximation to the modified Ping-Pong ball gun was not practical since the airflow in the gun exceeds the speed of sound. Therefore, the analytical prediction for only the basic Ping-Pong ball gun was verified.

Figure 4.27, 28, and 29 shows the results of the verification between the analytical prediction and the theoretical approximation for the basic model. Figure 30, 31, and 32 shows the results of the verification between the analytical prediction and the theoretical approximation for the basic_2 model. There was no significantly large difference between two results.

Figure 5.1 shows verification between the ball velocities along the pipe from analytical model analysis for the three different models. Table 5.1 shows the ball velocity of the three different models when the ball located at 0.025m and 0.05m. From the Table 5.1, the ball velocity was increased when modification from the basic model was applied. Table 5.2 shows that the increase of the ball velocity from the basic model to the basic_2 model and the basic_2 model to the modified model. At location 0.025m, the ball velocity of the basic_2 model increased 68.22% compare to the basic model. And the ball velocity of the modified model increased 22.58% compare to the basic_2 model. At location 0.05m, the ball velocity of the basic_2 model increased 75.78% compare to the basic model. And the ball velocity of the modified model increased 42.09% compare to the basic_2 model.

From this result, both the pressure difference and addition of the converging-diverging nozzle increased the ball velocity. However, the effect of the pressure difference was larger than the effect of the converging-diverging nozzle.

5.2 Future Work

An additional experimental study on the modified Ping-Pong gun test is required. The experimental results have to be obtained carefully since the test involves with high speed ball motion and airflow. The experimental results then are to be compared with the analysis results to verify the test results.

The fundamental behavior of the modified Ping-Pong gun test should be theoretically approximated. A new theoretical approach has to be derived.

Table 5.1 Ball velocity of three different analytical models when the ball located at 0.025m and 0.05m

	Ball velocity, m/s	
Model	x=0.025m	x=0.05m
Basic	45.7320	57.6794
Basic_2	76.9281	101.3883
Modified	94.2957	144.0580

Table 5.2 Increase of the ball velocity from basic model to basic_2 model and basic_2 model to modified model

	Increased, %	
Model	x=0.025m	x=0.05m
Basic → Basic_2	68.22	75.78
Basic_2→Modified	22.58	42.09

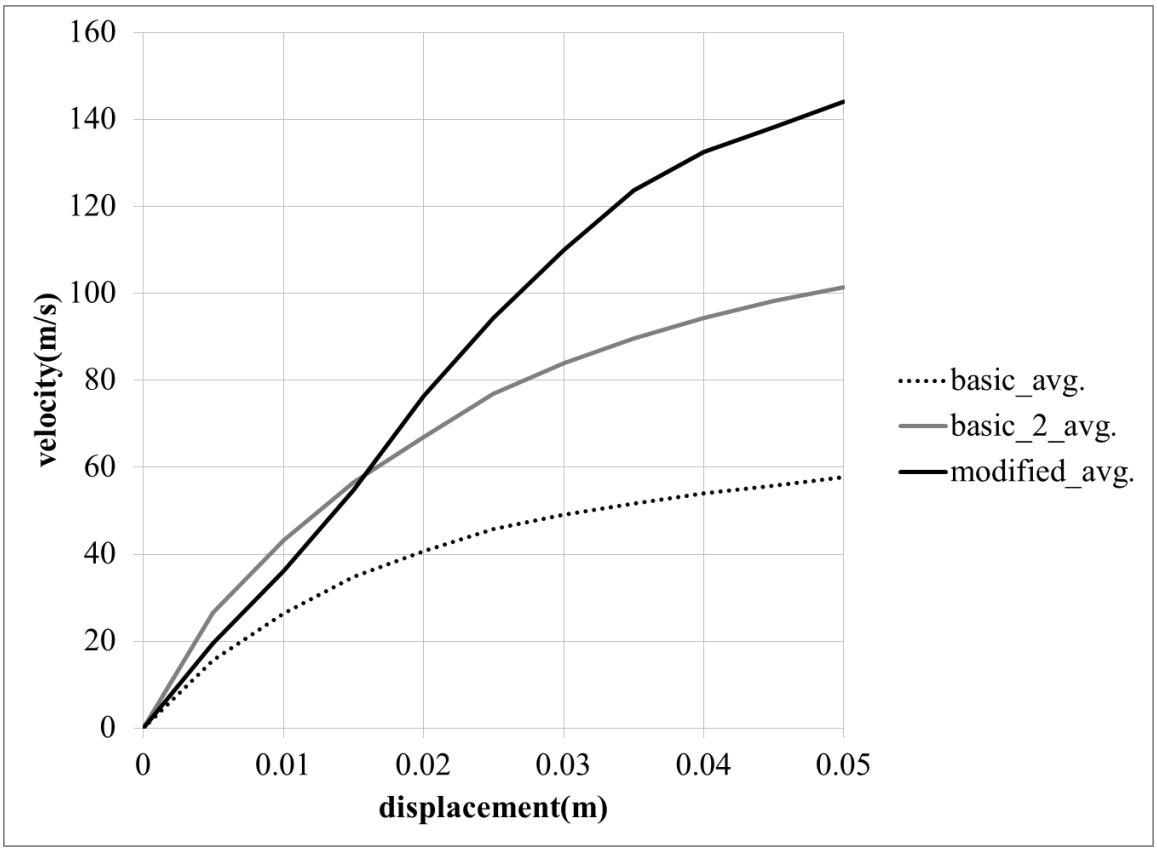

Figure 5.1 Analytical model results of the ball velocity for three different models.

LIST OF REFERENCES

LIST OF REFERENCES

Alpher, A. R., & White, D. R. (1957). "Flow in shock tubes with area change at the diaphragm section." *General Electric Research Laboratory*, (pp. 457-470). New York.

Ayars, E., & Buchholtz, L. (2004). "Analysis of the vacuum cannon." *American Journal of Physics*, 72(7), pp. 961-963.

Boyanapalli, R., Vanukuri, R., Gogineni, P., Nookala, J., Yarlagadda, G., & Gada, V. (2013). "Analysis of Composite De-Laval Nozzle Suitable for Rocket Applications." *International Journal of Innovative Technology and Exploring Engineering (IJITEE)*, pp. 336-344.

Chowdhury, M., Ahamed, J., Faruque, P., & Bhuiya, M. (2011, June). "Computational study of supersonic flow through a converging diverging nozzle." *Engineering e-Transaction*, pp. 1(6), 37-42.

Chung, T. J. (2002). *Computational Fluid Dynamics.* Cambridge: Cambridge University Press.

Cockman, J. (2003). "Improved Vacuum Bazooka." *The Physics Teacher*, 41(4), 246-247.

Downie, N. A. (2001). *Vacuum Bazookas, Electric Rainbow Jelly, and 27 Other Saturday Science Projects.* New Jersy: Princeton University Press

French, R. M., Gorrepati, V., Alcorta, E., & Jackson, M. (2008). "The Mechanics of a Ping-Pong Ball Gun." *Experimental Technique* , 24-30.

French, R. M., Zehrung, C., & Stratton, J. (2013). "A Supersonic Ping Pong Gun." *arXiv:1301.5188 [physics]*.

Kleinschmit, N. N. (2011). "A Shock Tube Technique for Blast Wave Simulation and Studies of Flow Structure Interactions in Shock Tube Blast Experiments." *DigitalCommons@University of Nebraska - Lincoln.*

Mungan, C. E. (2009). "Internal ballistics of a pneumatic potato cannon." *European Journal of Physics*, 30(3), 453.

Munson, B. R., Young, Okiishi, & Huebsch. (2009). *Fundamentals Of Fluid Mechanics, 6Th Ed, Si Version.* Wiley India Pvt. Limited.

Olson, G., Peterson, R., Pulford, B., Seaberg, M., Stein, K., Stelter, C., et al. (2006). "The role of shock waves in expansion tube accelerators." *American Journal of Physics*, 74(12), 1071-1076.

Ower, E., & Pankhurst, R. C. (1977). *The measurement of air flow.* New York: Pergamon Press.

Peterson, R. W., Pulford, B. N., & Stein, K. R. (2004). "The Ping-Pong Cannon: A Closer Look." *The Physics Teacher*, 43(1), 22-25.

Peyret, R., & Taylor, T. D. (1983). *Computational Methods for Fluid Flow.* New York: Springer-Verlag Inc.

Saad, M. A. (1985). *Compressible Fluid Flow.* New Jersey: Prentive-Hall INC.

Schreier, S. (1982). *Compressible Flow.* New York: John Wiley & Sons Inc.

Taylor, B. (2006). "Recoil Experiments Using a Compressed Air Cannon." *The Physics Teacher*, 44(9), 582-584.

White. (1995). *Fluid Mechanics.* New York: McGraw-Hill Inc.

White, F. M. (1991). *Viscous Fluid Flow.* New York: McGraw-Hill Inc.

Zucrow, M. J., & Hoffman, J. D. (1976). *Gas dynamics.* New York: Wiley.

APPENDIX

APPENDIX A

Theoretical Analysis of the Airflow for Basic Model

The airflow cause by the pressure difference in the pipe with uniform cross sectional area can be defined as ‘unsteady one-dimensional flow’ (Schreier, 1982). In gas dynamics, this problem is called a ‘shock tube’ problem. The shock tube is device in which a normal shock wave is produced by the sudden burst of a diaphragm that initially separates a gas at high pressure from a gas at low pressure(Schreier, 1982). The pipe is separated into two sections by the diaphragm. Figure A 1 shows the initial state of the shock tube. The pressure in section 4 is higher than in section 1. When the diaphragm is punctured, a shock wave forms instantaneously and propagates into section 1. Simultaneously, an expansion wave forms and propagates into section 4. Figure A 2 shows the phenomenon after the diaphragm is punctured. The high-pressure section (section 4) is called the driver, and the low-pressure section (section 1) is called the driven section (Schreier, 1982). Section 1, which is ahead of the propagating shock wave, is not yet influenced by the shock wave. Section 2, which is behind the propagating shock wave, is bounded by shock wave and diaphragm. The pressure, temperature and density of section 2 have been influenced by the propagating shock wave. Section 4, which is ahead of the propagating expansion fan, is not influenced by propagating expansion fan. Section 3, behind the propagating expansion fan, is bounded by the expansion fan and

the diaphragm. The pressure, temperature, and density of section 3 have been influenced by the propagating shock wave.

The relations across the shock wave (section 1 and 2) are given in Equation A l, A 2, and A 3.

$$\frac{u_2-u_1}{a_1} = \pm\frac{2}{\gamma+1}\left(M_x - \frac{1}{M_x}\right) \quad \text{(A 1)}$$

$$\frac{\rho_1}{\rho_2} = 1 - \frac{2}{\gamma+1}\left(1 - \frac{1}{M^2{}_x}\right) \quad \text{(A 2)}$$

$$\frac{p_2}{p_1} = 1 + \frac{2\gamma}{\gamma+1}(M^2{}_x - 1) \quad \text{(A 3)}$$

In Equation A 1, u_2 and u_1 are the velocity of the x-direction in section 1 and 2, γ is the specific heat ratio of the air, M_x is the Mach number of the shock wave. Equation A 2 shows the density ratio between section 1 and 2 where ρ_1 and ρ_2 are the density of section 1 and 2 respectively. Equation A 3 shows the pressure ratio between section 1 and 2 where p_1 and p_2 are the pressure of section 1 and 2 respectively.

With the given condition of $u_1 = 0$ and eliminating M_x from Equation A 1 and Equation A 3, Equation A 1 becomes Equation A 4.

$$\frac{u_2}{a_1} = \frac{\frac{p_2}{p_1}-1}{\gamma\sqrt{1+\frac{\gamma+1}{2\gamma}\left(\frac{p_2}{p_1}-1\right)}} \quad \text{(A 4)}$$

Now, the relations across the expansion fan (section 3 and 4) are given in Equation A 5.

$$\frac{u_3}{a_4} = \frac{2}{\gamma-1}\left(1 - \frac{a_3}{a_4}\right) = \frac{2}{\gamma-1}\left[1 - \left(\frac{p_3}{p_4}\right)^{(\gamma-1)/2\gamma}\right] \quad \text{(A 5)}$$

In Equation A 5, u_3 is the velocity of the x-direction in section 3, a_3 and a_4 are the speed of sound in section 3 and 4, p_3 and p_4 are the pressure of in section 3 and 4.

With the given condition of $u_4 = 0, u_3 = u_2, p_3 = p_2$ and assumption of $a_4 = a_1$, then, Equation A 4 becomes Equation A 6.

$$\frac{u_2}{a_1} = \frac{2}{\gamma - 1}\left[1 - \left(\frac{p_2}{p_1}\right)^{(\gamma-1)/2\gamma}\left(\frac{p_1}{p_4}\right)^{(\gamma-1)/2\gamma}\right] \tag{A 6}$$

Equating equations A 5 and A 6 then solving for p_1/p_4, the pressure ratio between section 1 and 4, p_1/p_4, is expressed as Equation A 7.

$$\frac{p_1}{p_4} = \frac{p_1}{p_2}\left[1 - \frac{\gamma-1}{2\gamma}\frac{\frac{p_2}{p_1}-1}{\sqrt{1+\frac{\gamma+1}{2\gamma}\left(\frac{p_2}{p_1}-1\right)}}\right]^{2\gamma/(\gamma-1)} \tag{A 7}$$

Equation A 7 shows the required ratio across the diaphragm for the desired pressure ratio across the shock (Schreier, 1982).

To obtain the value of M_x, consider the case of the fluid in section 1 and 4 is different (but, in this research, the fluid in section 1 and 4 is same, which is air). Also assumption of $u_3 = u_2, p_3 = p_2$, and $\gamma_1 = \gamma_2$, it is possible to rewrite Equation A 5 as Equation A 8 and Equation A 6 as Equation A 9.

$$\frac{u_3}{a_4} = \frac{2}{\gamma_4 - 1}\left[1 - \left(\frac{p_3}{p_4}\right)^{(\gamma_4-1)/2\gamma_4}\right] \tag{A 8}$$

$$\frac{u_2}{a_1} = \left[\frac{p_2}{p_1} - 1\right]\sqrt{\frac{2}{\gamma_1\left[(\gamma_1+1)\frac{p_2}{p_1}+(\gamma_1-1)\right]}} = \frac{2}{\gamma_1+1}\frac{{M^2}_x - 1}{M_x} \tag{A 9}$$

Combine Equation A 8 and A 9, the pressure ratio between section 1 and 4, p_1/p_4, is expressed as Equation A 10.

$$\frac{p_4}{p_1} = \frac{p_2}{p_1}\left[1 - \frac{a_1}{a_4}(\gamma_4 - 1)\frac{\frac{p_2}{p_1}-1}{\sqrt{2\gamma_1\left[(\gamma_1+1)\frac{p_2}{p_1}+(\gamma_1-1)\right]}}\right]^{-2\gamma_4/(\gamma_4-1)} \tag{A 10}$$

Recall the normal shock relation expressed as Equation A 11.

$$\frac{p_2}{p_1} = \frac{2\gamma_1}{\gamma_1+1} M^2{}_x - \frac{\gamma_1-1}{\gamma_1+1} \quad \text{(A 11)}$$

Substitute Equation A 11 into Equation A 10, Equation A 10 becomes Equation A 12.

$$\frac{p_4}{p_1} = \frac{1}{\gamma_1+1}(2\gamma_1 M^2{}_x + 1 - \gamma_1)\left[1 - \frac{a_1}{a_4}\left(\frac{\gamma_4-1}{\gamma_1+1}\right)\left(M_x - \frac{1}{M_x}\right)\right]^{-2\gamma_4/(\gamma_4-1)} \quad \text{(A 12)}$$

With these relationships, it is possible to calculate the shock wave Mach number of the basic model. The high-pressure region of the basic model is $p_4 = 1\text{atm}$ and the low-pressure region is $p_1 = 0.3\text{psi}$, so the pressure ratio between the two regions was approximately $\frac{p_4}{p_1} \approx 49$. γ_1 and γ_4 were the specific heat ratios of air, which was 1.4 respectively. Substituted the value of the pressure ratio and the specific heat ratio of air into Equation A 12 and the shock wave Mach number of the basic model is,

$$M_s = 2.1263$$

In this research, the pressure of section 1 is ideally vacuum condition, so it could be considered that $\frac{p_4}{p_1} \to \infty$ and M_x approaches a finite limit (Schreier, 1982). In conclusion, limiting the Mach number of the shock wave when $\frac{p_4}{p_1} \to \infty$ was

$$M_{x_{max}} = \frac{1}{2}\left(\frac{\gamma_1+1}{\gamma_4-1}\right)\frac{a_4}{a_1} + \sqrt{\left[\frac{1}{2}\left(\frac{\gamma_1+1}{\gamma_4-1}\right)\frac{a_4}{a_1}\right]^2 + 1} \quad \text{(A 13)}$$

Theoretical Analysis of the Airflow for Modified Model

It is inadequate to apply same theoretical analysis to the modified model that applied to the basic model. From the first-order approximation analysis of the basic model, there is a maximum velocity of the Ping-Pong ball. However, the Ping-Pong ball's terminal velocity in the modified model exceeds the theoretical maximum velocity of the basic model. It is a challenging problem to find the solution of the motion of the Ping-Pong ball for the modified model. According to the converging-diverging nozzle attached to the modified model, it is unsuitable to use the first-order approximation analysis based on Newton's second law of motion to predict the velocity of the ball. So in this section, the focus is on the pressure chamber and converging-diverging nozzle as part of the modified model and analyze on the theories related to it. First, the theoretical background of the converging-diverging nozzle will be introduced. Second, the explanation of the shock tube with area change will be analyzed. Third, analysis on the shock tube with converging-diverging nozzle will be introduced.

Converging-Diverging Nozzle (De Laval Nozzle)

A nozzle is a device that used to control fluid flow out of a chamber or pipe. For example, in rockets, the nozzle was used to maximize the thrust force. Expansion of internal energy and the pressure increase the flow of kinetic energy. The 'De Laval Nozzle' is not just a simple converging or diverging nozzle. It is shaped with a converging section at the front and a diverging section at the end. This converging-diverging nozzle was invented by 'Gustaf de Laval' in 1888 for use in steam turbines. The De Laval nozzle relies on the properties of supersonic flow to accelerate gas beyond

Mach 1. This nozzle is most widely used for the design of modern aerospace and rocketry applications and was implemented in rockets by 'Robert Goddard'.

Subsonic Inlet Case

In this section, the case of a subsonic inlet will be explained and specified into seven cases. Figure A 3 is diagram of De Laval nozzle showing approximate flow velocity with respect to temperature and pressure. Temperature and pressure drop as the Mach number of the fluid increases. To accelerate fluid over Mach 1, fluid must be choked at the throat of the nozzle. 'Choked' means that the fluid velocity at the throat reaches Mach 1. In chocked conditions, it is not possible to accelerate the fluid beyond Mach 1 at the throat by the increase of the pressure at the entrance. Acceleration over Mach 1 is only caused by a change in the back pressure or ambient pressure. Equation A 14 is the relation between the velocity change and the area change. Equation A 14 shows why the choked condition is require to occur for fluid to accelerate over Mach 1.

$$\frac{dV}{V} = \frac{1}{M^2-1}\frac{dA}{A} \tag{A 14}$$

If M^2 is less than 1, then dA must be negative to make dV positive. This means in subsonic inlet flow, reduction of area is required to accelerate the velocity of the fluid. In the case of supersonic inlet flow, area required to increase for acceleration to occur because M^2 is greater than 1 so dA must be positive for dV to be positive.

For the De Laval nozzle, the ratio between stagnation and nozzle exit pressure $\frac{p_e}{P_0}$ depends on the area ratio of the exit and the throat, $\frac{A_e}{A_0}$. Figure A 4 shows the scheme of

the converging-diverging nozzle and properties related to it. To obtain the equation of the area ratio, isentropic relations are required. It shows in Equation A 15, A 16, and A 17.

$$\frac{T_0}{T_e} = 1 + \frac{\gamma-1}{2} M_e{}^2 \quad \text{(A 15)}$$

$$\frac{P_0}{P_e} = (1 + \frac{\gamma-1}{2} M_e{}^2)^{\frac{\gamma}{\gamma-1}} \quad \text{(A 16)}$$

$$\frac{\rho_0}{\rho_e} = (1 + \frac{\gamma-1}{2} M_e{}^2)^{\frac{1}{\gamma-1}} \quad \text{(A 17)}$$

where, T_0, P_0 and ρ_0 are stagnation temperature, pressure and density respectively. M_e is the Mach number at the exit, and γ is specific heat ratio of the fluid.

From three isentropic relations, an equation of the exit and the throat area ratio is obtained as Equation A 18.

$$\frac{A_e}{A^*} = \frac{1}{M_e}\left[\frac{2}{\gamma+1}\left(1 + \frac{\gamma-1}{2} M_e{}^2\right)\right]^{\frac{\gamma+1}{2(\gamma-1)}} \quad \text{(A 18)}$$

The characteristics of the De Laval nozzle are specified to seven cases depending on the varying back pressure. Figure A 5 shows the characteristics of the De Laval nozzle. The pressure and the Mach number distribution along the nozzle of seven different cases are plotted in Figure A 5.

- Case (a): subsonic, un-choked flow.

  Figure A 6 shows the scheme of un-choked flow. Flow is not choked, and there is no shock wave through the nozzle. There is continuity in pressure, velocity, and temperature.

- Case (b): choked flow

Figure A 7 shows the scheme of choked flow. Subsonic flow shows downstream of the throat.

- Case (c): normal shock within nozzle

Figure A 8 shows the scheme of normal shock appeared within the nozzle. Isentropic flow upstream of shock and downstream of the shock is subsonic flow.

- Case (d): supersonic nozzle flow, normal shock at exit

Figure A 9 shows the scheme of normal shock appeared at the exit of the nozzle. Isentropic flow within nozzle, but need normal shock to get P_e to match P_b. The strongest normal shock occurs in this case.

- Case (e): supersonic over-expanded flow

Figure A 10 shows the scheme of over-expanded flow. An oblique shock shows outside of the nozzle.

- Case (f): supersonic design condition flow

Figure A 11 shows the scheme of supersonic design condition. It is perfectly expanded and supersonic flow at the exit. Flow is isentropic through the nozzle.

- Case (g): supersonic under-expanded flow

Figure A 12 shows the scheme of supersonic under-expanded flow. An expansion fan show outside of the nozzle. P_b is low, such that $P_e > P_b$ so flow must continue to expand flow to reach equilibrium with the surroundings.

Analysis of the flow characteristics of the De Laval nozzle is meaningful to find the optimized design of the nozzle and to reach the maximum efficiency.

Supersonic Inlet Case (Supersonic Diffuser)

In this case, the converging-diverging nozzle is assumed as a supersonic diffuser. Supersonic inlet flow of the converging-diverging nozzle is treated as a reversal of subsonic inlet flow. In this section, supersonic inlet flow is divided by four cases.

- Case (a): normal shock at the entrance

  Figure A 13 shows the scheme of the normal shock at the entrance of the nozzle.

- Case (b): normal shock at diverging section of nozzle

  Figure A 14 shows the scheme of the normal shock at the diverging section of the nozzle. Increase in Mach number of case (a), normal shock at the entrance becomes unstable so that the shock wave moves downstream of the nozzle and sits at the diverging section of the nozzle.

- Case (c): normal shock at nozzle throat

  Figure A 15 shows the scheme of the normal shock at the throat. Decrease in back pressure of case (b), ; shock wave moving towards the throat. Normal shock strength decreases.

- Case (d): no shock through nozzle

  Figure A 16 shows the scheme of no shock through the nozzle. Decreasing the in inlet Mach number of case (b) and adjusting back pressure properly, Mach

number in the throat of the nozzle is Mach 1. Isentropic subsonic flow in a diverging section of the nozzle is appeared.

Shock Tube with Area Change

In the last section, an analysis on the De Laval Nozzle was introduced in case of subsonic and supersonic inlet. In this section, an analysis about shock tube with area change will be conducted. In section 3.2, it was mentioned that the background theory of the basic model is a shock tube with a uniform area problem. However, the modified model has a converging-diverging nozzle attached to the pipe. Since the location of the diaphragm of the modified model is at the entrance of the converging-diverging nozzle, it will be assumed as a shock tube with area change. In case of the shock tube with area change is usually called a ‘shock tunnel’. This case is a shock tube with a continuous tube sufficiently small in diameter. Analysis of the shock tube with a converging-diverging nozzle will be introduced in the next section.

Figure A 17 (a) represents the initial condition before the shock hits the neck of the tube. Figure A 17 (b) shows the one part of the shock in which continuous flow through the narrower tube and the rest of the part reflected back to the wider tube. Th e strength of the Reflected and continuous shock is weaker than the original shock (Schreier, 1982). Following the continuous shock, there is an interface which separates the fluid that already passed through the continuous shock and the fluid that already passed through the reflected shock (Schreier, 1982). The effect of area change is approximated as the quasi-steady-state analysis (Schreier, 1982). If consider area change acting as a converging nozzle, it is impossible to accelerate the flow over Mach 1.

However, if the shock wave is strong enough to generate the supersonic flow in the narrower tube, a rarefaction wave is generated which accelerates the flow to reach the final velocity in region 3. The velocity of the left end of the rarefaction wave is $u = a$, and the wave is stationary at the entrance of the narrow tube(Schreier, 1982). The right end of the rarefaction wave velocity is $u - a$ (Schreier, 1982). The purpose of using this type of device is to increase the pressure and test time.

Shock Tube with Converging-Diverging Nozzle

It is assumed that the driven force of the Ping-Pong ball is generated by the shock tube with the converging-diverging nozzle. This kind of device is called a 'shock tube driven wind tunnel'. In this section, an analysis on the effect of the shock tube flow through the converging-diverging nozzle will be conducted. The stronger shock wave is generated by the shock tube having an area reduction transforming a high-pressure region to a low-pressure region compare to the shock tube having an uniform area (Alpher & White, 1957). In this section, the procedures of calculating fluid properties through the converging-diverging nozzle will be introduced.

Figure A 18 showS a schematic drawing of shock tube with converging-diverging nozzle. Assumptions of this analysis are isentropic flow except across the shock wave and ideal gas condition. Recall the relationship between the pressure ratio $\frac{p_4}{p_1}$, $\frac{p_2}{p_1}$, and the shock wave Mach number M_s for the shock tube with uniform area in Equation A 10, A 11, and A 12.

$$\frac{p_4}{p_1} = \frac{p_2}{p_1}\left[1 - \frac{a_1}{a_4}(\gamma_4 - 1)\frac{\frac{p_2}{p_1} - 1}{\sqrt{2\gamma_1\left[(\gamma_1+1)\frac{p_2}{p_1} + (\gamma_1 - 1)\right]}}\right]^{-2\gamma_4/(\gamma_4-1)} \quad \text{(A 10)}$$

$$\frac{p_2}{p_1} = \frac{2\gamma_1}{\gamma_1+1}{M_s}^2 - \frac{\gamma_1-1}{\gamma_1+1} \quad \text{(A 11)}$$

$$\frac{p_4}{p_1} = \frac{1}{\gamma_1+1}(2\gamma_1{M_s}^2 + 1 - \gamma_1)\left[1 - \frac{a_1}{a_4}\left(\frac{\gamma_4-1}{\gamma_1+1}\right)\left(M_s - \frac{1}{M_s}\right)\right]^{-2\gamma_4/(\gamma_4-1)} \quad \text{(A 12)}$$

With these relationships, it is possible to calculate the shock wave Mach number of the modified model. The high-pressure region of the modified model is $p_4 = 4atm$ and the low pressure region is $p_1 = 0.3psi$, so the pressure ratio between the two regions is approximately $\frac{p_4}{p_1} \approx 196$. γ_1 and γ_4 are the specific heat ratio of air, which is 1.4. The value of the pressure ratio and the specific heat ratio of air are substituted into Equation A 12. The shock wave Mach number of modified model Is,

$$M_s = 2.6029$$

Now, consider the general case of the converging-diverging nozzle section. When the shock wave flow is generated, the pressure ratio of region 4 and region 1, $\frac{p_4}{p_1}$ is expanded as Equation A 19 (Alpher & White, 1957).

$$\frac{p_4}{p_1} = \frac{p_4}{p_{3a}}\frac{p_{3a}}{p_{3b`}}\frac{p_{3b`}}{p_{3b}}\frac{p_{3b}}{p_3}\frac{p_3}{p_2}\frac{p_2}{p_1} \quad \text{(A 19)}$$

where $\frac{p_4}{p_{3a}}$ is the pressure ratio required to accelerate the low-pressure region fluid by unsteady expansion from zero to M_{3a}. $\frac{p_{3a}}{p_{3b`}}$ is the required pressure ratio to proceed the low pressure region fluid by steady expansion from $M_{3a}$ to $M_{3b`}$. According to the flow

from region 3b` to 3b (steady, supersonic, or subsonic), the flow at 3b` become a sonic condition or not. $\frac{p_{3b`}}{p_{3b}}$ is the pressure ratio required to make flow from $M_{3b`}$ to M_{3b} a steady expansion form. Pressure ratio $\frac{p_{3b}}{p_3}$ is required for unsteady expansion flow from M_{3b} to M_3. At the interface, $p_3 = p_2$, and pressure ratio $\frac{p_2}{p_1}$ defines the shock strength (Alpher & White, 1957). Rewrite Equation A 19 as Equation A 20.

$$\frac{p_4}{p_1} = \left\{\left[1 + \frac{\gamma_4 - 1}{2} M_{3a}\right]\left[\frac{2+(\gamma_4-1){M_{3b}}^2}{2+(\gamma_4-1){M_{3a}}^2}\right]^{1/2}\left[\frac{2+(\gamma_4-1)M_3}{2+(\gamma_4-1)M_{3b}}\right]\right\}^{2\gamma_4/(\gamma_4-1)} \qquad \text{(A 20)}$$

Equation A 20 showS the relationship among M_3, M_{3a}, and M_{3b} as well as $\frac{p_4}{p_1}$ and $\frac{p_2}{p_1}$. However, additional relationships are necessary. Region 3b` is the minimum cross-sectional area of the converging-diverging nozzle (Alpher & White, 1957). Whether $M_{3b`}$ is subsonic or supersonic, the area the ratio between region 4 and region 1 is expressed as Equation A 21.

$$\frac{A_4}{A_1} = \frac{M_{3b}}{M_{3a}}\left[\frac{2+(\gamma_4-1){M_{3a}}^2}{2+(\gamma_4-1){M_{3b}}^2}\right]^{(\gamma_4+1)/2(\gamma_4-1)} \qquad \text{(A 21)}$$

Another required relationship is connection between M_s with M_3, M_{3a} and M_{3b}. This relationship show in Equation A 22.

$$M_3 = \left[\frac{a_1}{v_2}\frac{a_4}{a_1} g^{(\gamma_4-1)/2\gamma_4} - \frac{\gamma_4-1}{2}\right]^{-1} \qquad \text{(A 22)}$$

where

$$\frac{v_2}{a_1} = \left[\frac{2}{\gamma_4+1}\frac{{M_S}^2-1}{M_S}\right]^{-1} \qquad \text{(A 23)}$$

g is an 'equivalence' factor. It is defined as Equation A 24.

$$g = \left\{ \left[\frac{2+(\gamma_4-1){M_{3a}}^2}{2+(\gamma_4-1){M_{3b}}^2} \right]^{1/2} \left[\frac{2+(\gamma_4-1)M_{3b}}{2+(\gamma_4-1)M_{3a}} \right] \right\}^{2\gamma_4/(\gamma_4-1)} \quad \text{(A 24)}$$

Using equivalence factor g, rearrange the Equation A 20 as Equation A 25.

$$\frac{p_4}{p_1} = \frac{p_2}{p_1}\frac{1}{g}\left[1 + \frac{\gamma_4-1}{2}M_3\right]^{2\gamma_4/(\gamma_4-1)} = \frac{p_2}{p_1}\frac{1}{g}\left[1 - \frac{v_2}{a_1}\frac{a_1}{a_4}\frac{\gamma_4+1}{2}g^{-(\gamma_4-1)/2\gamma_4}\right]^{-2\gamma_4/(\gamma_4-1)} \quad \text{(A 25)}$$

Since the pressure ratio $\frac{p_4}{p_1}$, the area ratio $\frac{A_4}{A_1}$, and the shock wave Mach number M_s are given, it is possible to calculate the Mach numbers inside the converging-diverging nozzle with Equation A 21 through A 25.

Subsonic Flow

In this case, the converging-diverging section is a subsonic nozzle with conditions of $M_3 = M_{3b}$, $p_3 = p_{3b}$ and $a_3 = a_{3b}$. Rearrange the equation A 21, A 22, and A 24 and calculate M_3 and M_{3a} with known properties of a_1, a_4, $\frac{A_4}{A_1}$, and M_s (Alpher & White, 1957).

Supersonic Flow

Since $M_3 \geq 1$, a sufficient condition for supersonic flow through converging-diverging nozzle is $M_{3b`} = 1$ (Alpher & White, 1957).

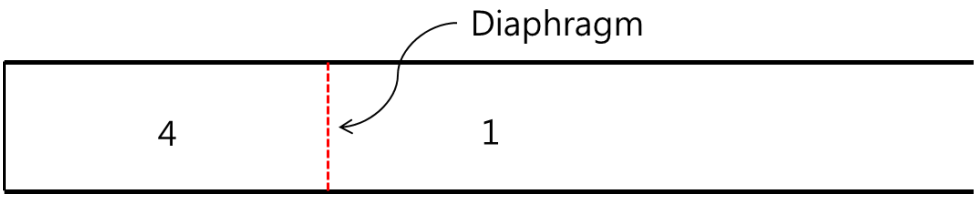

Figure A 1 Schematic drawing of shock tube

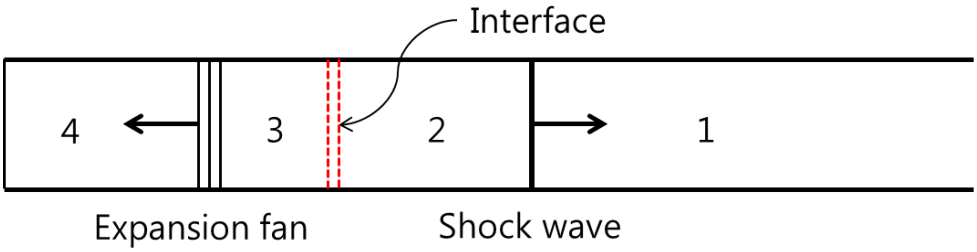

Figure A 2 Schematic drawing of the wave pattern in shock tube

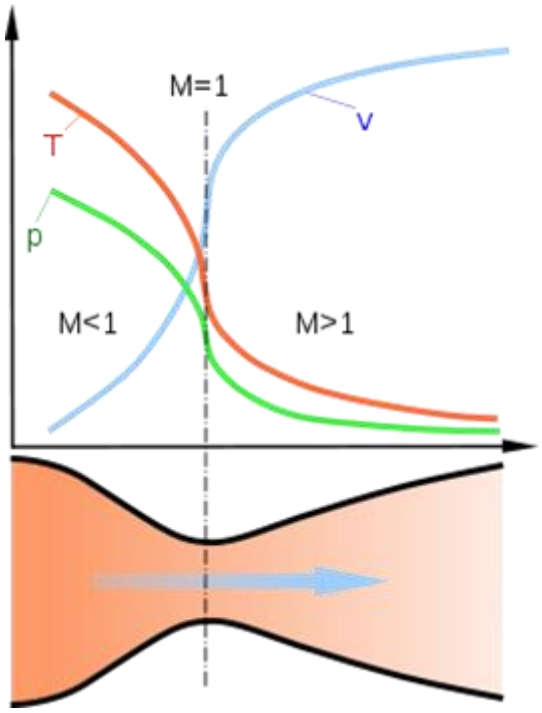

Figure A 3 Diagram of De Laval nozzle

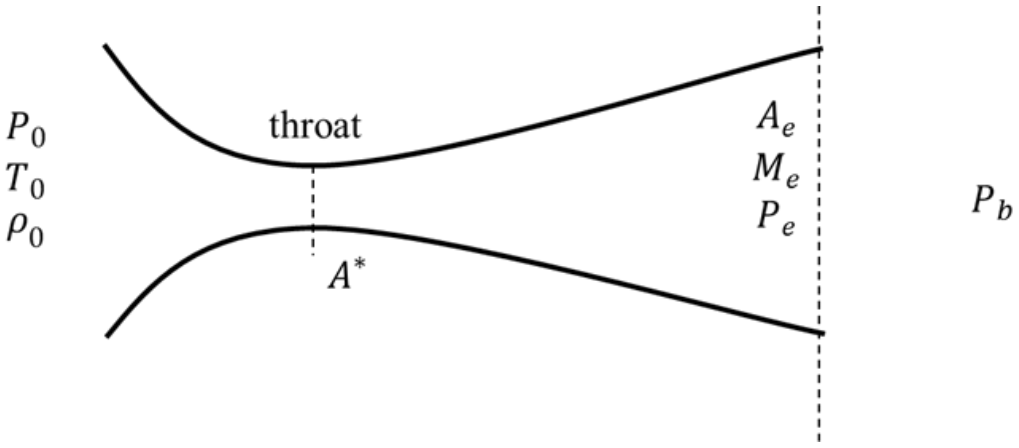

Figure A 4 Scheme of converging-diverging nozzle

v

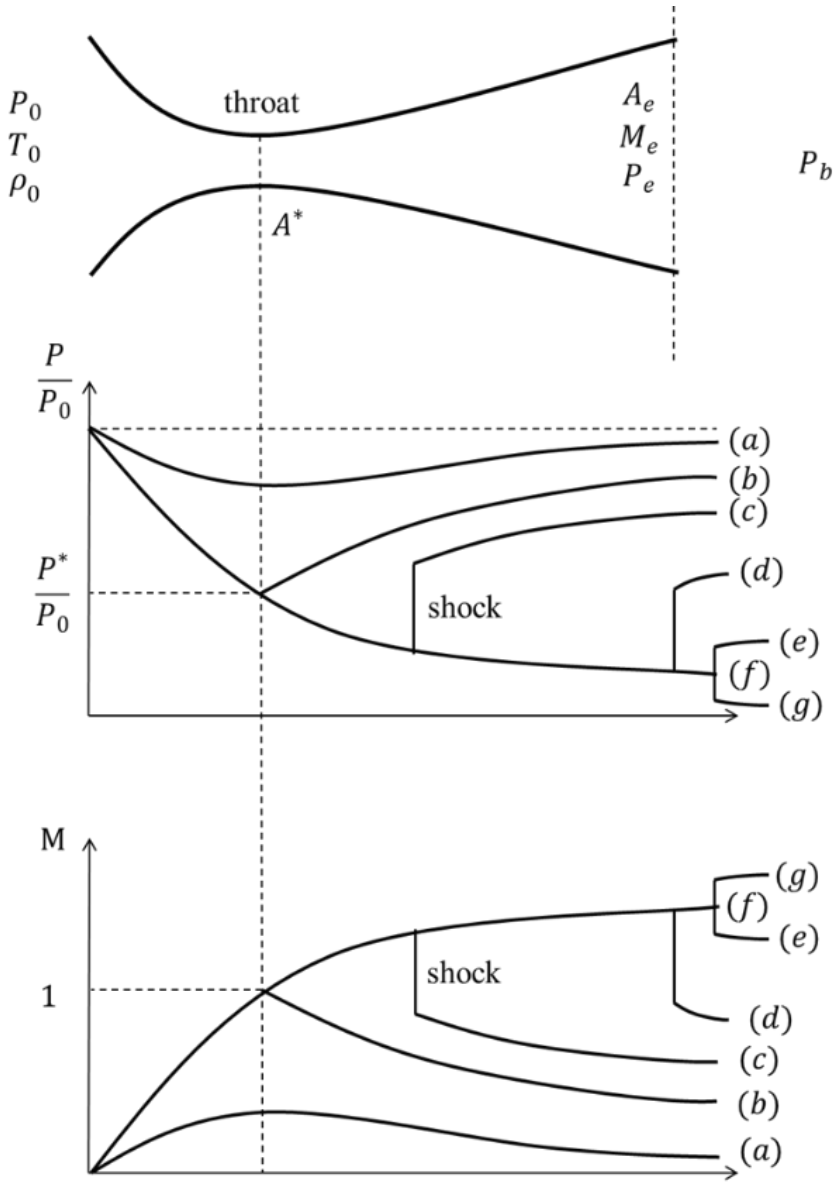

Figure A 5 Characteristics of converging-diverging nozzle(subsonic inlet)

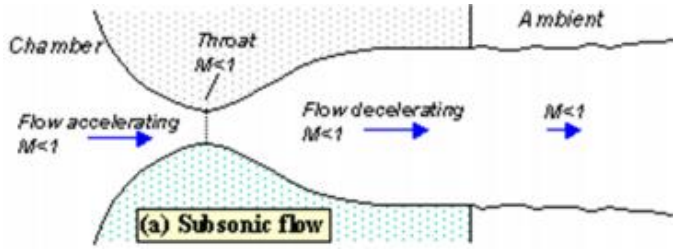

Figure A 6 Subsonic flow

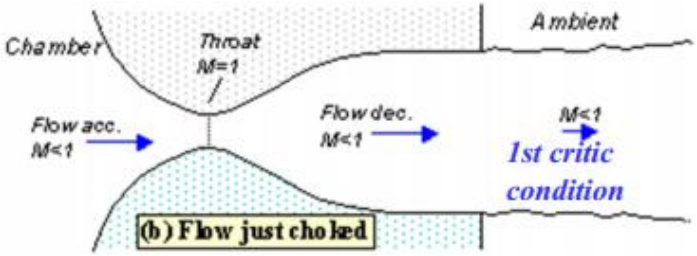

Figure A 7 Choked flow

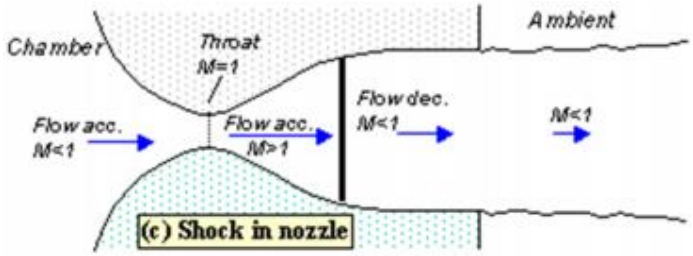

Figure A 8 Shock in nozzle

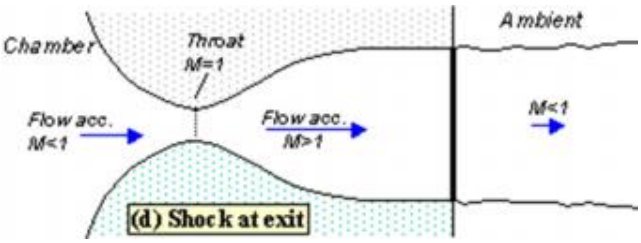

Figure A 9 Shock at exit

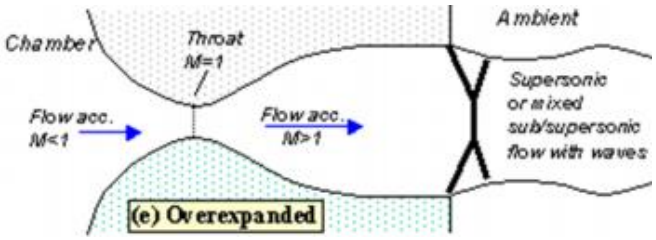

Figure A 10 Over-expanded

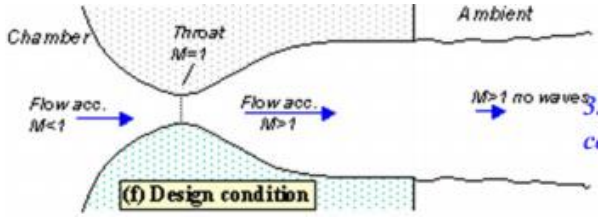

Figure A 11 Design condition

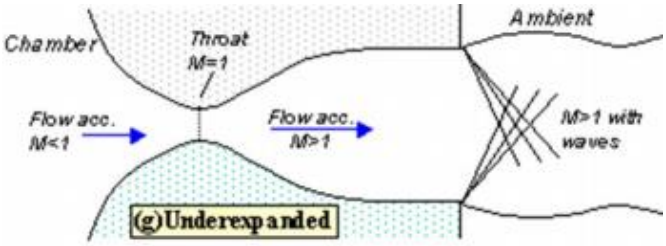

Figure A 12 Under-expanded

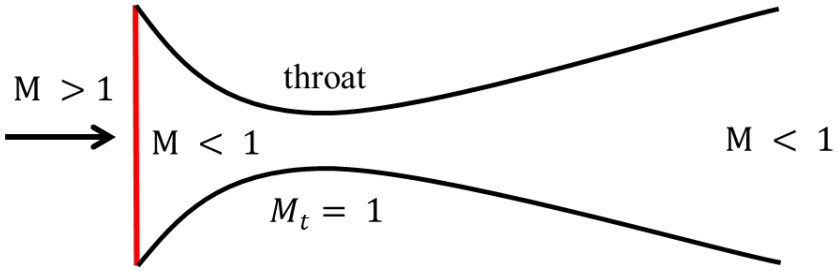

Figure A 13 Shock at entrance

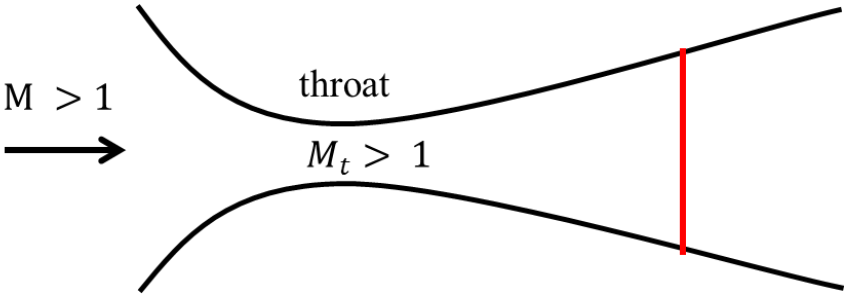

Figure A 14 Shock in nozzle

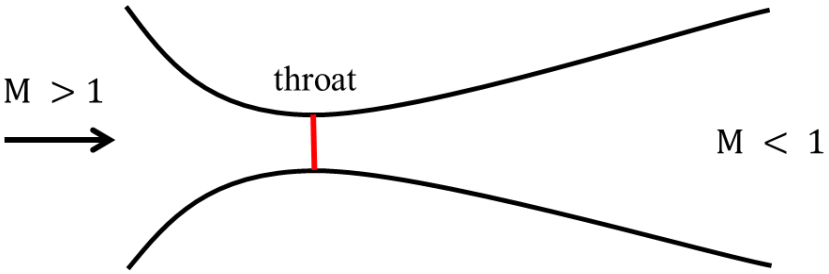

Figure A 15 Shock at nozzle throat

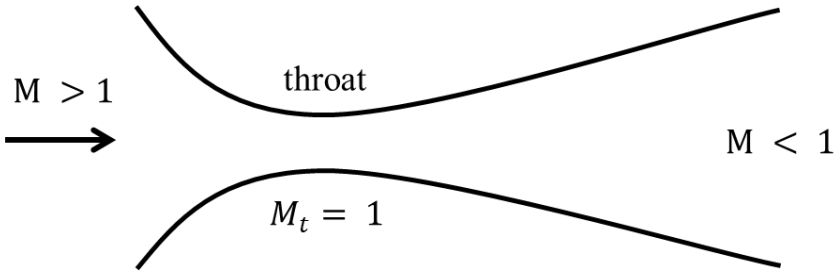

Figure A 16 No shock

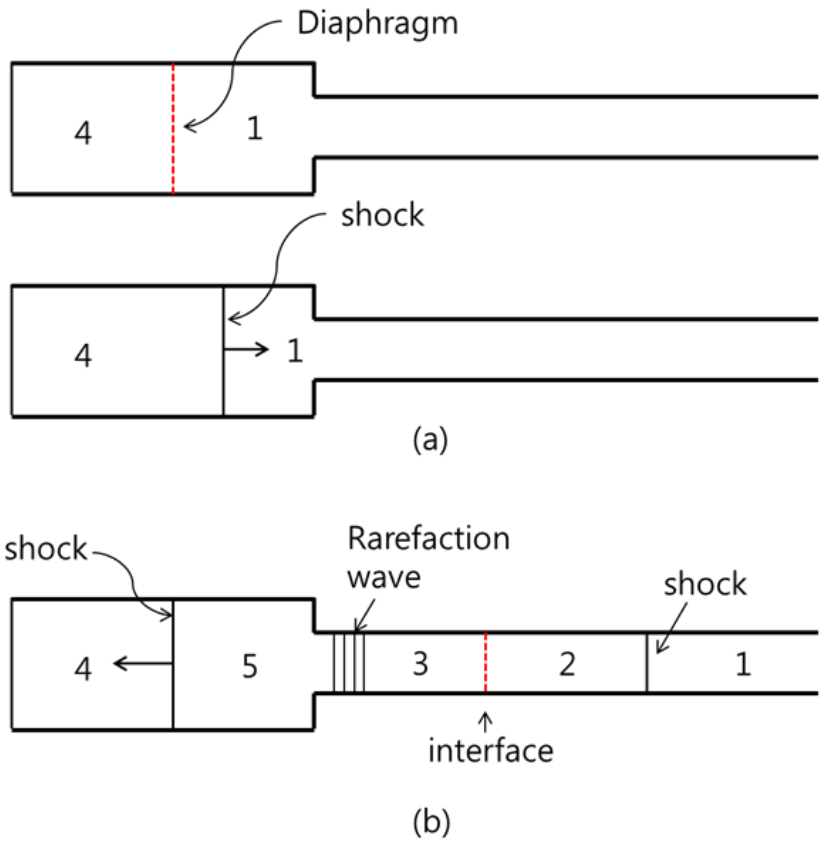

Figure A 17 (a) Before and right after shock generated (b) After shock reflected at the neck of the shock tube

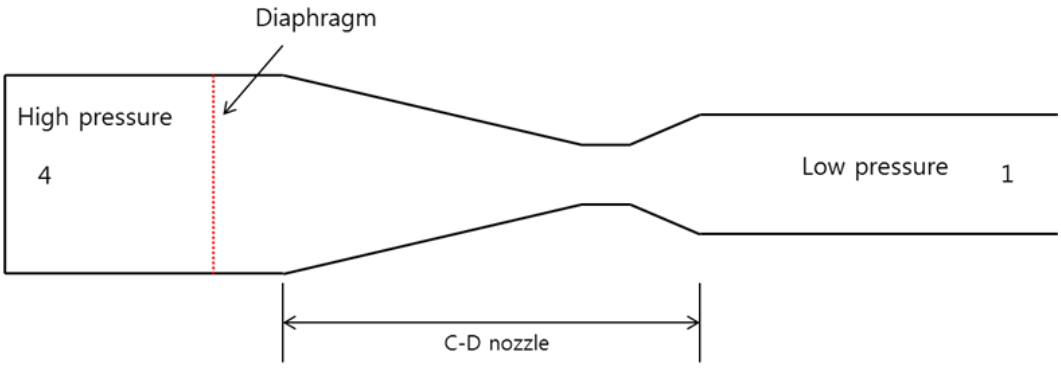

Figure A 18 Initial condition of shock tube with converging-diverging nozzle

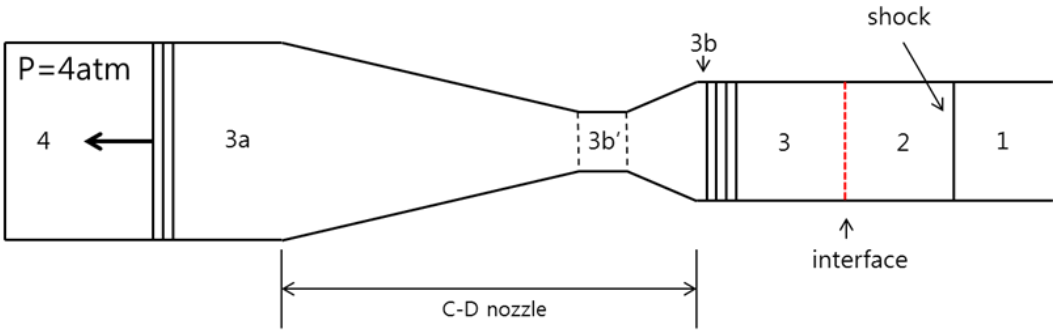

Figure A 19 After shock wave generated

VITA

VITA

Jun Han Bae
College of Technology, Purdue University

Education

B.S., Mechanical Engineering, 2011, Yonsei University, Seoul, Republic of Korea
M.S., Technology, 2014, Purdue University, West Lafayette, Indiana